EPJ manuscript No.
(will be inserted by the editor)

Methods to Determine Neutrino Flux at Low Energies:

Investigation of the Low ν Method

A. Bodek[1], U. Sarica[1], D. Naples[2] and L. Ren[2]

[1] Department of Physics and Astronomy, University of Rochester, Rochester, NY 14627-0171 USA
[2] University of Pittsburgh, Pittsburgh, PA 15260

Received: date / Revised version: date Jan 11, 2012

Abstract. We investigate the low ν method (developed by the CCFR/NUTEV collaborations) to determine the neutrino flux in a wide band neutrino beam at very low energies, a region of interest to neutrino oscillations experiments. Events with low hadronic final state energy $\nu < \nu_{cut}$ (of 1, 2 and 5 GeV) were used by the MINOS collaboration to determine the neutrino flux in their measurements of neutrino (ν_μ) and antineutrino ($\bar{\nu}_\mu$) total cross sections. The lowest ν_μ energy for which the method was used in MINOS is 3.5 GeV, and the lowest $\bar{\nu}_\mu$ energy is 6 GeV. At these energies, the cross sections are dominated by inelastic processes. We investigate the application of the method to determine the neutrino flux for ν_μ,$\bar{\nu}_\mu$ energies as low as 0.7 GeV where the cross sections are dominated by quasielastic scattering and $\Delta(1232)$ resonance production. We find that the method can be extended to low energies by using ν_{cut} values of 0.25 and 0.50 GeV, which is feasible in fully active neutrino detectors such as MINERvA.

PACS. 13.60.Hb Total and inclusive cross sections (including deep-inelastic processes) – 13.15.+g Neutrino interactions

1 Introduction

A detailed understanding of neutrino (ν_μ) and antineutrino ($\bar{\nu}_\mu$) interaction cross sections for various final states is required for the next generation neutrino oscillations experiments. The relevant neutrino energy region of interest for the large neutrino detectors such as T2K[1], MINOS[2, 3], and NOVA[4] is $0.5 < E_\nu < 3$ GeV.

The MINERvA[5] experiment at the NUMI wide band beam at Fermilab uses a fine grain fully active scintillator target-detector to investigate neutrino (ν_μ) and antineutrino ($\bar{\nu}_\mu$) cross sections for energies above 0.5 GeV. These measurements require a reliable determination of the flux as a function of ν_μ,$\bar{\nu}_\mu$ energy.

Previous neutrino experiments in wide band beams utilized three methods for the determination of flux as a function of energy.

1. Modeling the production of pions and kaons in the interactions of the incident proton beam in the target, and tracking the pions and kaons though the Horn focussing magnetic fields, followed by modeling of pion, kaon and muon decays in the decay pipe.
2. Measuring the muon flux that exit the decay pipe and relating it to the neutrino flux.
3. The low ν method for the determination of the energy dependence of the relative neutrino and antineutrino flux.

Here, low ν refers to events with low energy transfer to the target nucleon in the scattering processes $\nu_\mu + N \rightarrow \mu^- X$ and $\bar{\nu}_\mu + N \rightarrow \mu^+ X$. This energy transfer manifests itself as the energy ($\nu = E_{had}$) of the final state hadrons (X) in the laboratory frame.

There are inherent difficulties in the first two techniques:

1. For method 1, the differential cross sections for the production of pions and kaons by protons incident on a thick nuclear target must be known very well. In addition, the magnetic field of the horn focussing magnets must be modeled reliably.
2. For method 2, the response of the muon detectors at the end of the decay pipe must be very well understood (for absolute calibration of the neutrino flux). The response of the muon detectors is sensitive to δ rays. In addition, since the energy of the muons is not measured, it is difficult to determine the energy dependence of the neutrino flux.

Consequently, having a third independent technique such as the "low-ν" method is extremely valuable.

The "low-ν" method was initially developed by the CCFR/NUTEV [6,7] collaboration. At high energy, the method was used to determine the relative neutrino flux as a function of neutrino energy (E_ν). The method relies on the observation that the charged current differential cross section, $\frac{d\sigma^{\nu,\bar{\nu}}}{d\nu}$ in the limit $\nu \rightarrow 0$, only depends on

the structure function $\mathcal{F}_2$, and therefore is independent of energy.

The "low-ν" method was used by the CCFR/NuTeV collaborations to measure the energy dependence of σ_ν/E and $\sigma_{\bar{\nu}}/E$ for charged current interactions for energies higher than 30 GeV for an iron target. The absolute level of the charged cross sections is normalized to previous measurements of σ_ν/E in a high energy narrow band neutrino beam.

Most recently, the method was extended to lower energies by the MINOS [3] collaboration. The lowest neutrino energy for which this method was used in MINOS is 3.5 GeV for neutrinos and 6 GeV for antineutrinos.

The absolute normalization used by MINOS is to the world average values of charged current σ/E measurements for an isoscaler target for neutrino energies between 30 to 50 GeV. The average values used by MINOS are

$$\langle \sigma_\nu/E \rangle_{30-50} = 0.675 \times 10^{-38} cm^2/GeV$$

per nucleon, and

$$\langle \sigma_{\bar{\nu}}/E \rangle_{30-50} = 0.329 \times 10^{-38} cm^2/GeV$$

per nucleon .

In this communication we investigate the application of the technique to much lower neutrino energies ($E_\nu >$ 0.5 GeV). Neutrino interactions in this energy range are currently being studied at MINERvA.

2 The low ν method at high energies

If we neglect terms which are proportional to the muon mass, the differential cross section $\frac{d^2\sigma^{\nu,\bar{\nu}}}{dxdy}$ for charged current scattering of ν_μ ($\bar{\nu}_\mu$) with an incident energy E_ν, muon final energy E_μ and scattering angle θ can be written in terms of the structure functions $\mathcal{F}_1 = M\mathcal{W}_1(x,Q^2)$, $\mathcal{F}_2 = \nu\mathcal{W}_2(x,Q^2)$ and $\mathcal{F}_3 = \nu\mathcal{W}_3(x,Q^2)$:

$$\frac{d^2\sigma^{\nu(\bar{\nu})}}{dxdy} = \frac{G_F^2 M E_\nu}{\pi}\Big(\Big[1 - y(1+\frac{Mx}{2E_\nu}) + \frac{y^2}{2}\Big(\frac{1+(\frac{2Mx}{Q})^2}{1+R}\Big)\Big]\mathcal{F}_2 \pm \Big[y - \frac{y^2}{2}\Big]x\mathcal{F}_3\Big), \quad (1)$$

where G_F is the Fermi weak coupling constant, M is the proton mass, $y = \nu/E_\nu$ where $\nu = E_{had} = E_\nu - E_\mu$, $Q^2 = 4E_\nu E_\mu \sin^2(\theta/2)$ is the square of four momentum transfer, and $x = Q^2/(2M\nu)$ is the Bjorken scaling variable.

Here, $R_L(x,Q^2)$ is defined as the ratio of the longitudinal and transverse structure functions (σ_L/σ_T). It is related to the other structure functions by,

$$R(x,Q^2) = \frac{\sigma_L}{\sigma_T} = \frac{\mathcal{F}_2}{2x\mathcal{F}_1}(1+\frac{4M^2x^2}{Q^2}) - 1 = \frac{\mathcal{F}_L}{2x\mathcal{F}_1} \quad (2)$$

where $\mathcal{F}_L$ is called the longitudinal structure function.

$$\mathcal{F}_L(x,Q^2) = \mathcal{F}_2\left(1+\frac{4M^2x^2}{Q^2}\right) - 2x\mathcal{F}_1 \quad (3)$$

Other useful relations are:

$$2x\mathcal{F}_1 = \mathcal{F}_2\left(1+\frac{4M^2x^2}{Q^2}\right) - \mathcal{F}_L(x,Q^2). \quad (4)$$

$$2x\mathcal{F}_1(x,Q^2) = \mathcal{F}_2(x,Q^2)\frac{1+4M^2x^2/Q^2}{1+R(x,Q^2)}$$

$$\mathcal{W}_1(x,Q^2) = \mathcal{W}_2(x,Q^2)\frac{1+\nu^2/Q^2}{1+R(x,Q^2)}$$

The three structure functions $\mathcal{F}_2(x,Q^2)$, $\mathcal{F}_1(x,Q^2)$ and $x\mathcal{F}_3(x,Q^2)$ depend on x and Q^2. The plus sign in front of the xF_3 term is for neutrinos and the minus is for antineutrinos.

Integrating over x, the differential dependence on ν can be written in the simplified form

$$\frac{d\sigma^{\nu,\bar{\nu}}}{d\nu} = A\left(1 + \frac{B}{A}\frac{\nu}{E_\nu} - \frac{C}{A}\frac{\nu^2}{2E_\nu^2}\right). \quad (5)$$

The coefficients A, B, and C depend on integrals over structure functions, where

$$A = \frac{G_F^2 M}{\pi}\int_0^1 \mathcal{F}_2(x)dx, \quad (6)$$
$$B = -\frac{G_F^2 M}{\pi}\int_0^1 \Big(\mathcal{F}_2(x) \mp x\mathcal{F}_3(x)\Big)dx,$$
$$C = B - \frac{G_F^2 M}{\pi}\int_0^1 \mathcal{F}_2(x)\ \tilde{R}\ dx,$$

where

$$\tilde{R} = \left(\frac{1+\frac{2Mx}{\nu}}{1+R_L} - \frac{Mx}{\nu} - 1\right).$$

In the limit $\nu/E_\nu \to 0$, the A term dominates and the B and C terms are very small. The MINOS collaboration used the number of low ν events (with $\nu < \nu_{cut}$) in the detector to determine the relative flux of neutrinos and antineutrinos as a function of E_ν.

In the MINOS analysis, the relative flux is determined using events with $\nu < 1$ GeV for ν_μ energies in the range $3 < E_\nu < 9$ GeV, and for $\bar{\nu}_\mu$ in the range $5 < E_\nu < 9$ GeV. Events with $\nu < 2$ GeV are used for ν_μ and $\bar{\nu}_\mu$ events in the range $9 < E_\nu < 18$ GeV, and events with $\nu < 5$ GeV are used for $E_\nu > 18$ GeV.

MINOS divides the number of low ν events with $y < y_{cut} = \nu_{cut}/E_\nu$ by correction term f_C to account for the energy dependence from the B and C terms. Here

$$f_C = 1 + \int_0^{y_{cut}} \frac{B}{A}\frac{\nu}{E_\nu}dy - \int_0^{y_{cut}} \frac{C}{A}\frac{\nu^2}{2E_\nu^2}dy \quad (7)$$

As seen in equation 6, the negative contribution of $\mathcal{F}_2(x)$ in B partially cancels the positive contribution of $x\mathcal{F}_3(x)$ for ν_μ's. For $\bar{\nu}_\mu$'s both contributions are negative. There

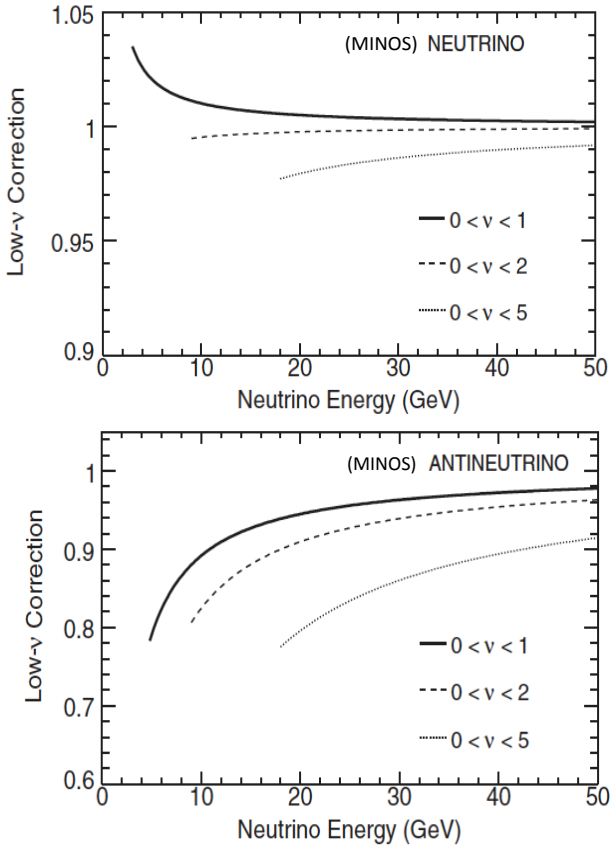

Fig. 1. The low ν correction factors f_C used by MINOS for neutrinos (shown in the top panel) and antineutrinos (shown in the bottom panel) (color online).

are additional small corrections that are applied to equation 6 to correct for differences in charm production between neutrinos and antineutrinos.

Equivalently, f_C can we written as

$$f_C = \frac{\sigma(\nu < \nu_{cut}, E)}{\sigma(\nu < \nu_{cut}, E = \infty)} \quad (8)$$

In practice, a neutrino interaction generator model [**?**] is used to compute f_C from Eq. 7. The corrections factors f_C used by MINOS for ν_μ and $\bar{\nu}_\mu$ are shown in Fig. 1.

The measured low ν sample is corrected for detector smearing and acceptance by multiplying the number of observed low ν events in the data, $N^{DATA}(E_{reconstructed}, \nu < \nu_{cut})$ by

$$R^{MC}(E) = \frac{N^{GEN}(E_{reconstructed}, \nu < \nu_{cut})}{N^{REC}(E_{reconstructed}, \nu < \nu_{cut})},$$

which is obtained from a Monte Carlo detector simulation. $N^{GEN}(E_{reconstructed}, \nu < \nu_{cut})$ and $N^{REC}(E_{reconstructed}, \nu < \nu_{cut})$ are the number of generated and reconstructed events below ν_{cut} in each reconstructed energy bin, respectively. In the first pass the initial input flux from a beam model is used. It is then replaced by the extracted low ν flux and the procedure is reiterated to account for the effect of the flux model on the acceptance corrections. (The change in the extracted flux is found to be negligible). MINOS corrects this acceptance corrected low ν sample for radiative effects using Ref. [9]. The absolute level of the flux is set by normalizing the cross section in data to a nominal world average charged current cross section at some high energy. As mentioned earlier, in MINOS the normalization is set to the average of previous σ_{total}/E measurements for neutrino energies between 30 and 50 GeV.

There are three criteria for the effectiveness of the low ν method.

1. The number of low ν events that are used in the determination of the flux should not be a large fraction of the total number of neutrino events in each energy bin.
2. The systematic uncertainty in the energy dependent correction factor f_C should be small.
3. The number of low ν events that are used in the determination of the flux should be sufficiently large to to have flux sample with small statistical errors.

The first two criteria require a ν_{cut} which is as low as possible. The third requires a ν_{cut} which is as large as possible.

The MINOS collaboration uses the criteria that the fractional contribution of events with $\nu < \nu_{cut}$ to the total charged current cross section should be less than 60%. MINOS uses events with $\nu < 1$ GeV for determination of the flux at their lowest $\nu_\mu, \bar{\nu}_\mu$ energies.

The fraction of events with $\nu < 1$ GeV is less than 60% for ν_μ interactions with $E_\nu > 3$ GeV and for $\bar{\nu}_\mu$ interactions with $E_{\bar{\nu}} > 5$ GeV. Therefore, to determine the flux for $E_\nu < 3$ GeV and $E_{\bar{\nu}} < 5$ GeV we need to use a ν_{cut} which is smaller than 1 GeV.

We investigate $\nu_{cut} = 0.25$ GeV to be used for $E_{\nu,\bar{\nu}} > 0.7$ GeV, and $\nu_{cut} = 0.5$ GeV to be used for $E_{\nu,\bar{\nu}} > 1.4$ GeV. These samples can be cross calibrated against the $\nu_{cut} = 1$ GeV sample in the range $E_\nu > 3$ GeV for neutrinos and $E_{\bar{\nu}} > 5$ GeV for antineutrinos. Similarly, they can be calibrated against the $\nu_{cut} = 2$ GeV and $\nu_{cut} = 5$ GeV samples in the range $E_{\nu,\bar{\nu}} > 9$ GeV and $E_{\nu,\bar{\nu}} > 18$ GeV, respectively.

3 The low ν method at low energies

In the few GeV region, the are several types of neutrino interaction processes as defined by the final state invariant mass W. These include quasielastic (QE) reactions ($W < 1.07$ GeV), production of the $\Delta(1232)$ resonance ($1.1 < W < 1.4$ GeV), coherent pion production, production of higher mass resonances ($1.4 < W < 2.0$ GeV) and the inelastic continuum ($W > 2.0$ GeV).

Fig. 2 shows the accessible kinematic region in Q^2 (in GeV^2 and $\nu = E_{had}$ (in GeV) for $E_\nu < 4$ GeV. Fig. 3 shows the accessible kinematic region in Q^2 and ν for $E_\nu < 1.5$ GeV.

For E_ν= 3 GeV, about 1/3 of the total charged current cross section originates from QE scattering, 1/3 from resonance production and 1/3 from inelastic scattering.

As seen in Fig. 3 the $\nu < 0.25$ GeV sample is dominated almost entirely by QE events with $Q^2 < 0.45$ GeV^2.

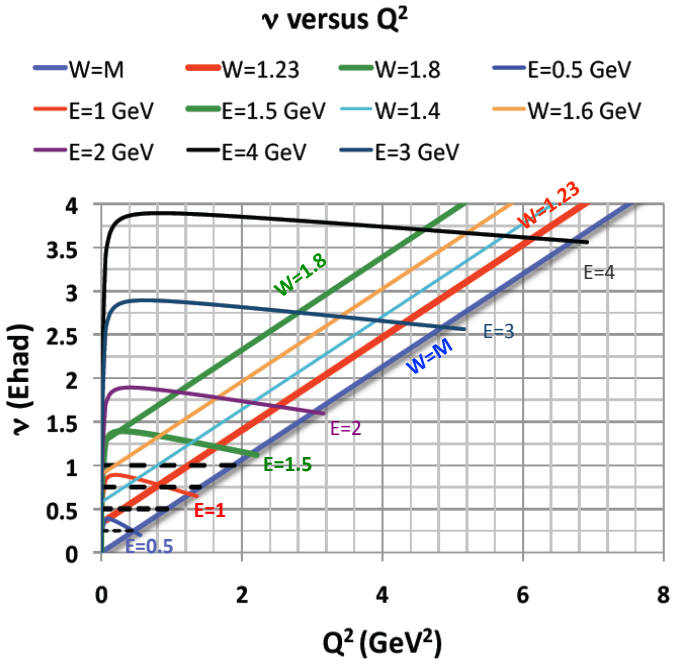

Fig. 2. The accessible kinematic region in the Q^2 (in GeV^2), $\nu = E_{had}$ (in GeV) plane for ν_μ ($\bar{\nu}_\mu$) energies less than 4 GeV (color online).

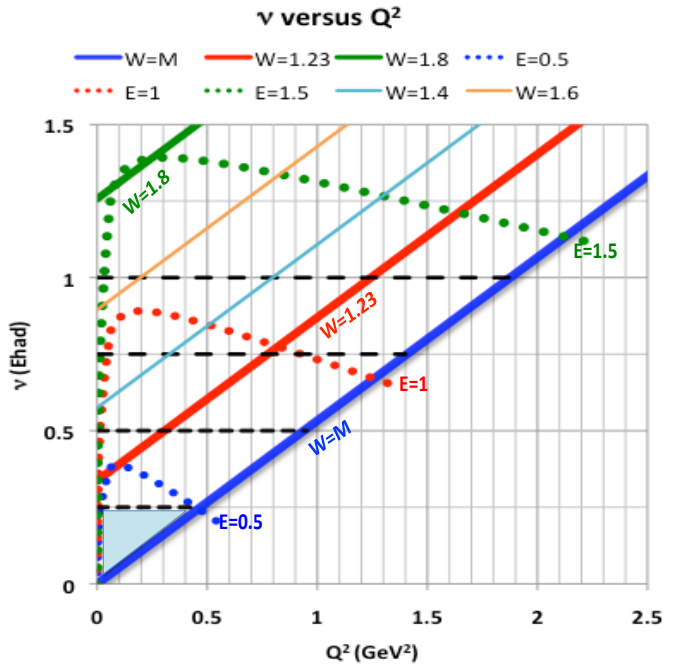

Fig. 3. The accessible kinematic region in the Q^2 (in GeV^2), $\nu = E_{had}$ (in GeV) plane for ν_μ ($\bar{\nu}_\mu$) energies less than 1.5 GeV (color online).

The $\nu < 0.5\ GeV$ sample includes both QE events with $Q^2 < 0.95$ GeV^2 and also $\Delta(1232)$ resonance events with $Q^2 < 0.3$ GeV^2. Both samples includes a very small fraction of events originating from coherent pion production.

In the low ν region it is more convenient to write the expression for the charged current differential cross sections as follows[10,11]:

$$\frac{d^2\sigma}{dQ^2 d\nu} = S_{cos}\frac{1}{2E^2}\mathcal{W}_1\left[Q^2 + m_\mu^2\right] + S_{cos}\mathcal{W}_2\left[(1-\frac{\nu}{E}) - \frac{(Q^2+m_\mu^2)}{4E^2}\right] + S_{cos}\mathcal{W}_3\left[\frac{Q^2}{2ME} - \frac{\nu}{4E}\frac{Q^2+m_\mu^2}{ME}\right] + S_{cos}\mathcal{W}_4\left[m_\mu^2\frac{(Q^2+m_\mu^2)}{4M^2E^2}\right] - S_{cos}\mathcal{W}_5\left[\frac{m_\mu^2}{ME}\right] \quad (9)$$

where $S_{cos} = \frac{G^2}{2\pi}\cos^2\theta_C = 80\times10^{-40}\ cm^2/GeV^2$. In the scattering process, there are additional small contributions from strangeness and charm non-conserving processes. In the discussion below we do not show these terms explicitly, but charm and strangeness changing contributions are assumed to be included in the analysis. (The strangeness changing valence quark contributions are proportional to $\frac{G^2}{2\pi}\sin^2\theta_C$).

Each of the structure functions has a vector and axial component (except for $\mathcal{W}_3$ which originates from axial-vector interference). The vector part of $\mathcal{W}_4$ and $\mathcal{W}_5$ are well known since they are related to the vector part of $\mathcal{W}_2$ and $\mathcal{W}_1$ by the following expressions[10]:

$$\mathcal{W}_4^{vector} = \mathcal{W}_2^{vector}\frac{M^2\nu^2}{Q^4} - \mathcal{W}_1^{vector}\frac{M^2}{Q^2}$$
$$\mathcal{W}_5^{vector} = \mathcal{W}_2^{vector}\frac{M\nu}{Q^2}$$

At low ν and very high energy the charged current cross section is only a function of $\mathcal{W}_2$. If we integrate the cross section from $\nu_{min} \approx 0$ up to $\nu = \nu_{cut}$ (where ν_{cut} is small), we can write the expression for the cross section in terms of $\mathcal{W}_2$ only, and energy dependent corrections ratios to the $\mathcal{W}_2$ component:

$$\int_{\nu_{min(E)}}^{\nu_{cut}}\frac{d^2\sigma}{dQ^2 d\nu}dQ^2 d\nu = \sigma_{W_2} + \sigma_2 + \sigma_1 + \sigma_3 + \sigma_4 + \sigma_5$$

where we integrate the cross section up to $\nu < \nu_{cut}$ (of 0.25 or 0.5 GeV or kinematic limit). Here, $\sigma_{W_2} \approx \sigma_{W_2}(\infty)$, where

$$\sigma_{W_2} = S_{cos}\int_{\nu_{min(E)}}^{\nu_{cut}}\mathcal{W}_2\ d\nu. \quad (10)$$

$$\sigma_{W_2}(\infty) = S_{cos}\int_{\nu_{min(E=\infty)}}^{\nu_{cut}}\mathcal{W}_2\ d\nu. \quad (11)$$

and the small corrections to the QE cross section are:

$$\sigma_2 = S_{cos} \int_{\nu_{min(E)}}^{\nu_{cut}} \left[-\frac{\nu}{E} - \frac{Q^2 + m_\mu^2}{4E^2} \right] \mathcal{W}_2 \; d\nu$$

$$\sigma_1 = S_{cos} \int_{\nu_{min(E)}}^{\nu_{cut}} - \left[\frac{(Q^2 + m_\mu^2)}{2E^2} \right] \mathcal{W}_1 \; d\nu$$

$$\sigma_3 = S_{cos} \int_{\nu_{min(E)}}^{\nu_{cut}} \left[\frac{Q^2}{2ME} - \frac{\nu}{4E} \frac{Q^2 + m_\mu^2}{ME} \right] \mathcal{W}_3 \; d\nu$$

$$\sigma_4 = S_{cos} \int_{\nu_{min(E)}}^{\nu_{cut}} \left[m_\mu^2 \frac{(Q^2 + m_\mu^2)}{4M^2E^2} \right] \mathcal{W}_4 \; d\nu$$

$$\sigma_5 = S_{cos} \int_{\nu_{min(E)}}^{\nu_{cut}} \left[\frac{-m_\mu^2}{ME} \right] \mathcal{W}_5 \; d\nu \qquad (12)$$

The above can be written in terms of fractional corrections:

$$\sigma_{\nu cut}(E) = \sigma_{W_2}(\infty) \, [f_C]$$

$$f_C = [f_{W2} + f_2 + f_1 + f_3 + f_4 + f_5]$$

$$f_{W2} = \frac{\sigma_{W2}}{\sigma_{W_2}(\infty)} (\approx 1)$$

$$f_2 = \frac{\sigma_2}{\sigma_{W_2}(\infty)} (= kinematic \; correction)$$

$$f_1 = \frac{\sigma_1}{\sigma_{W_2}(\infty)} (= important)$$

$$f_3 = \frac{\sigma_3}{\sigma_{W_2}(\infty)} (= important)$$

$$f_4 = \frac{\sigma_4}{\sigma_{W_2}(\infty)} (= very \; small)$$

$$f_5 = \frac{\sigma_4}{\sigma_{W_2}(\infty))} (= very \; small) \qquad (13)$$

The energy dependent corrections f_{W2}, f_1, f_2, f_3, f_3, and f_4 and f_5 can be calculated within a specific models. The theoretical uncertainty in f_C determines the systematic uncertainty in the relative flux which can extracted from the low ν events.

1. $f_{W2} = \frac{\sigma_{W2}}{\sigma_{W_2}(\infty)} \approx 1$ is well known and does not contribute to the uncertainty in f_C.
2. The energy dependent correction f_2 is purely kinematic and therefore does not contribute to the uncertainty in f_C.
3. The contributions of f_4 and f_5 are small since they are proportional to the square of the muon mass, and therefore have a negligible contribution to the uncertainty in f_C. (Note that the vector parts of f_4 and f_5 are known very well since they can be expressed in terms of the vector parts of $\mathcal{W}_1$ and $\mathcal{W}_2$).
4. The only non-negligible uncertainty originates from the modeling of the contributions of f_1 and f_3 (primarily from f_3).

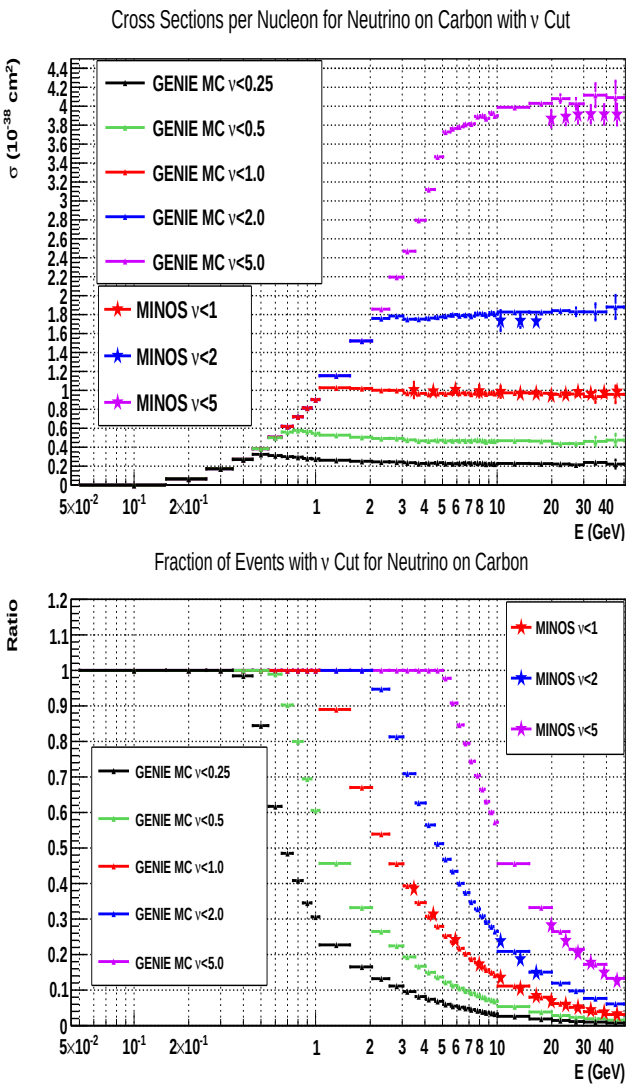

Fig. 4. Top panel: Neutrino partial charged cross sections per nucleon for low ν events (for ν cuts of 0.25, 0.5, 1, 2 and 5 GeV) as a function of energy determined from the GENIE Monte Carlo[12] for a carbon target. Also shown are the measurements of MINOS on iron (for ν cuts of 1, 2 and 5 GeV). Bottom panel: The fraction of low ν neutrino events in the GENIE[12] Monte Carlo as compared with the measurements of MINOS. The MINOS cross sections for iron has been corrected for the excess number of neutrons in iron (color online).

The technique does not depend on the modeling of $\mathcal{W}_2$ because the σ_{W_2} cross section is the same at all energies. All energy dependent corrections are expressed in terms of ratios to σ_{W_2}. In quark parton language, the uncertainty in f_1 is related to the uncertainty in the longitudinal structure function at low Q^2 and the uncertainty in f_3 is related to the uncertainty in level of antiquarks in the nucleon at low Q^2. For QE scattering and resonance production the structure functions are expressed in terms of form factors.

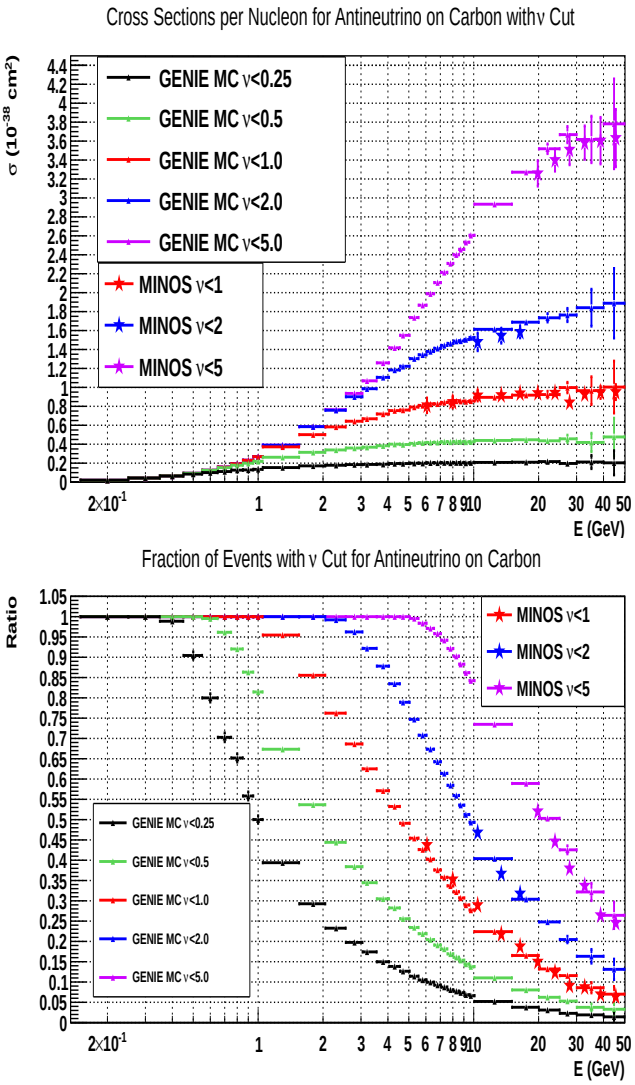

Fig. 5. Top panel: Antineutrino partial charged cross sections per nucleon for low ν events (for ν cuts of 0.25, 0.5, 1, 2 and 5 GeV) as a function of energy determined from the GENIE[12] Monte Carlo for a carbon target. Also shown are the measurements of MINOS on iron (for ν cuts of 1, 2 and 5 GeV). Bottom panel: The fraction of low ν antineutrino events in the GENIE Monte Carlo as compared with the measurements in MINOS. The MINOS cross sections for iron has been corrected for the excess number of neutrons in iron (color online).

3.1 Partial charged current cross sections

The top panel of Fig. 4 shows the partial neutrino charged current cross section per nucleon for low ν events (for ν cuts of 0.25, 0.5, 1, 2 and 5 GeV) as a function of energy as determined by the GENIE[12] Monte Carlo for a carbon target. The top panel of Fig. 5 shows the corresponding partial charged current cross sections for antineutrinos.

Also shown are the measurements of the partial charged current cross sections on iron from the MINOS collaboration (for ν cuts of 1, 2 and 5 GeV). The MINOS cross sections for iron has been corrected for the excess number of neutrons in iron. Note that the partial cross sections on carbon and on iron can be somewhat different.

At high energies (as shown in Fig. 4 and 5) the partial cross sections for a fixed ν_{cut} are independent of energy and are approximately equal for neutrinos and antineutrino. The fact that these partial charged current cross section are relatively independent of energy is the basis for the low ν method.

The bottom panels of figures 4 and 5 show the fraction of low ν events predicted by the GENIE Monte Carlo as compared with the measurements in MINOS. In order to use the technique at low energies the fractions must be smaller than 0.6. Therefore, at the lowest energies we must use ν cuts of 0.25 and 0.50 GeV.

MINOS is a sampling target calorimeter which has poor resolution at low hadron energy. Therefore, low ν samples with $\nu < 0.25\ GeV$ and $\nu < 0.5\ GeV$ cannot be defined reliably. On the other hand, since the MINERvA detector is a fully active target calorimeter, low ν samples with $\nu < 0.25\ GeV$ and $\nu < 0.5\ GeV$ can be used.

3.2 Absolute normalization

Since the neutrino energy range for MINERvA is limited to lower energies, we propose that the MINERvA charged current cross section measurements be normalized to the cross section in the energy range between 10 to 20 GeV (e.g. at a mean energy of 15.1 GeV). The absolute level of the charged current cross section at this energy range has been measured by both the MINOS and NOMAD collaborations.

The MINOS total cross section measurement for an isoscalar iron target at a neutrino energy of 15.1 GEV is

$$\sigma_{\nu}^{MINOS}/E = 0.708 \pm 0.020 \times 10^{-38} cm^2/GeV$$

per nucleon in iron. Here the total error of 0.02 is the combined statistical, systematic and normalization errors of $0.008 \pm 0.012 \pm 0.015$, respectively.

The NOMAD cross section measurement for an isoscalar carbon target at a neutrino energy of 15.1 GEV is

$$\sigma_{\nu}^{NOMAD}/E = 0.698 \pm 0.025 \times 10^{-38} cm^2/GeV$$

per nucleon in carbon.

The MINOS total cross section measurement for an isoscalar iron target at an antineutrino energy of 15.1 GEV is

$$\sigma_{\bar{\nu}}^{MINOS}/E = 0.304 \pm 0.012 \times 10^{-38} cm^2/GeV$$

per nucleon in iron. Here, the total error of 0.012 is the combined statistical, systematic and normalization errors of $0.007 \pm 0.007 \pm 0.006$, respectively.

Alternatively, it may be possible for MINERvA to normalize to the partial cross sections measured by MINOS for $\nu < 1\ GeV$ and $\nu < 2\ GeV$ at 15.1 GeV. These partial cross sections (which were used by MINOS to determine their relative flux) are relatively constant between 10 and 20 GeV. However, the MINOS partial cross sections are

measured on iron. The MINERvA target is solid scintillator (i.e. carbon), and the partial cross sections for iron and carbon can be different. For a neutrino energy of 15.1 GeV MINOS measured the following isoscalar partial cross sections on iron (per nucleon).

$$\sigma_{\nu}^{MINOS}(15.1) = 1.729 \pm 0.049 \times 10^{-38} cm^2 (\nu < 2\ GeV)$$

$$\sigma_{\nu}^{MINOS}(15.1) = 0.968 \pm 0.027 \times 10^{-38} cm^2 (\nu < 1\ GeV)$$

For an antineutrino energy of 15.1 GeV MINOS has measured the following isoscalar partial cross sections on iron (per nucleon).

$$\sigma_{\bar{\nu}}^{MINOS}(15.1) = 1.585 \pm 0.063 \times 10^{-38} cm^2 (\nu < 2\ GeV)$$

$$\sigma_{\bar{\nu}}^{MINOS}(15.1) = 0.939 \pm 0.039 \times 10^{-38} cm^2 (\nu < 1\ GeV)$$

4 Using low ν events with $\nu < 0.25\ GeV$

As seen in Fig. 3 the $\nu < 0.25$ region is dominated by QE events. This is illustrated in Fig. 6 which shows the relative contributions of QE and non-QE processes to $\nu < 0.25\ GeV$ cross section as a function of energy (as determined from the GENIE Monte Carlo). The $\nu < 0.25\ GeV$ cross sections for ν_μ are shown on the top panel, and the $\nu < 0.25\ GeV$ cross sections for $\bar{\nu}_\mu$ are shown on the bottom panel. The QE contribution is shown in red, the contribution from pion production process (e.g. Δ, inelastic and coherent pion) is shown in blue and and the total is shown in black. Most of the events are QE and the contribution from pion production processes is negiligible.

As mentioned earlier, the technique does not rely the modeling of $\mathcal{W}_2$, or the modeling of nuclear effects (e.g. Fermi motion smearing) on $\mathcal{W}_2$. This is because the cross section σ_{W_2} (including nuclear effects) is the same at all neutrino energies.

The uncertainty in the flux extracted from the event sample with $\nu < 0.25\ GeV$ is determined by how well we can model the relative contributions of $\mathcal{W}_1$ and $\mathcal{W}_3$ for the case of QE scattering on bound nucleons, or equivalently the relative contributions of f_1 and f_3 to f_C. Here f_1 and f_3 are proportional to the ratios $\frac{\mathcal{W}_1}{\mathcal{W}_2}$ and $\frac{\mathcal{W}_3}{\mathcal{W}_2}$. Since the ratios $\frac{\mathcal{W}_1}{\mathcal{W}_2}$ and $\frac{\mathcal{W}_3}{\mathcal{W}_2}$ for QE scattering on free nucleons are very well known, the uncertainty in f_C originates primarily from modeling the nuclear corrections to $\frac{\mathcal{W}_1}{\mathcal{W}_2}$ and $\frac{\mathcal{W}_3}{\mathcal{W}_2}$ for nucleons bound in a nuclear target.

4.1 Quasielastic $\nu_\mu, \bar{\nu}_\mu$ scattering

The relationship between the structure functions and form factors for $\nu_\mu, \bar{\nu}_\mu$ QE scattering[13] on free nucleons is given by[14,15]:

$$W_{1-Qelastic}^{\nu-vector} = \delta(\nu - \frac{Q^2}{2M})\tau |\mathcal{G}_M^V(Q^2)|^2$$

$$W_{1-Qelastic}^{\nu-axial} = \delta(\nu - \frac{Q^2}{2M})(1+\tau)|\mathcal{F}_A(Q^2)|^2$$

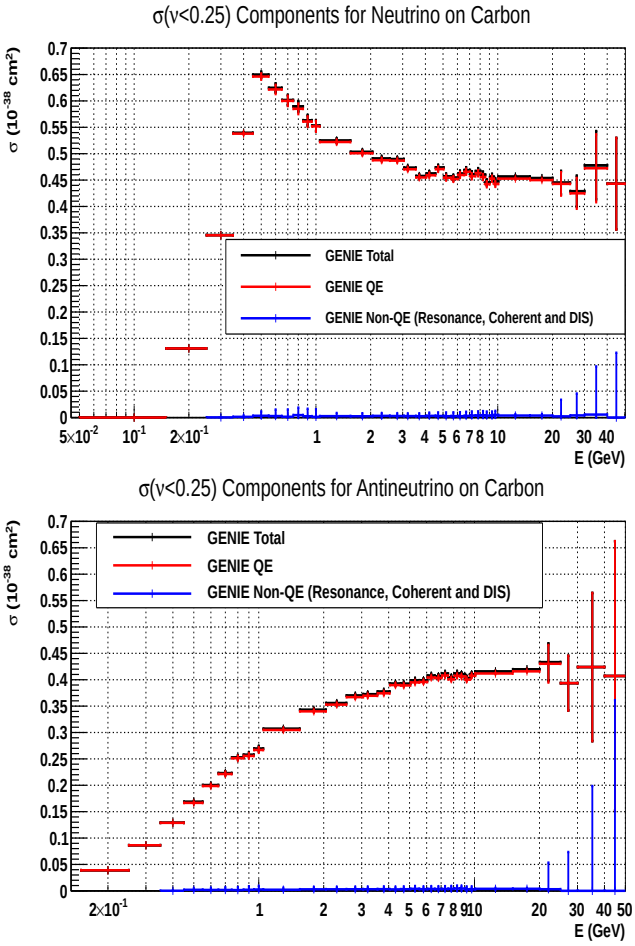

Fig. 6. The $\nu < 0.25\ GeV$ partial charged current cross sections (per nucleon) as a function of energy from the GENIE Monte Carlo (for carbon target). Shown are the QE contribution, the contribution from pion production process (e.g. Δ, inelastic and coherent pion) and the total. The $\nu < 0.25\ GeV$ cross sections for ν_μ are shown on the top panel, and the $\nu < 0.25\ GeV$ cross sections for $\bar{\nu}_\mu$ are shown on the bottom panel. Most of the $\nu < 0.25\ GeV$ events are QE and only a very small contribution is from pion production processes (color online).

$$W_{2-Qelastic}^{\nu-vector} = \delta(\nu - \frac{Q^2}{2M})|\mathcal{F}_V(Q^2)|^2$$

$$W_{2-Qelastic}^{\nu-axial} = \delta(\nu - \frac{Q^2}{2M})|\mathcal{F}_A(Q^2)|^2$$

$$W_{3-Qelastic}^{\nu} = \delta(\nu - \frac{Q^2}{2M})|2\mathcal{G}_M^V(Q^2)\mathcal{F}_A(Q^2)|$$

$$W_{4-Qelastic}^{\nu-vector} = \delta(\nu - \frac{Q^2}{2M})\frac{1}{4}(|\mathcal{F}_V(Q^2)|^2 - |\mathcal{G}_M^V(Q^2)|^2)$$

$$W_{4-Qelastic}^{\nu-axial} = \delta(\nu - \frac{Q^2}{2M}) \times \frac{1}{4} \times$$

$$\left[\mathcal{F}_A^2(Q^2) + (\frac{Q^2}{M^2} + 4)|\mathcal{F}_p(Q^2)|^2 - (\mathcal{F}_A(Q^2) + 2\mathcal{F}_P(Q^2))^2\right]$$

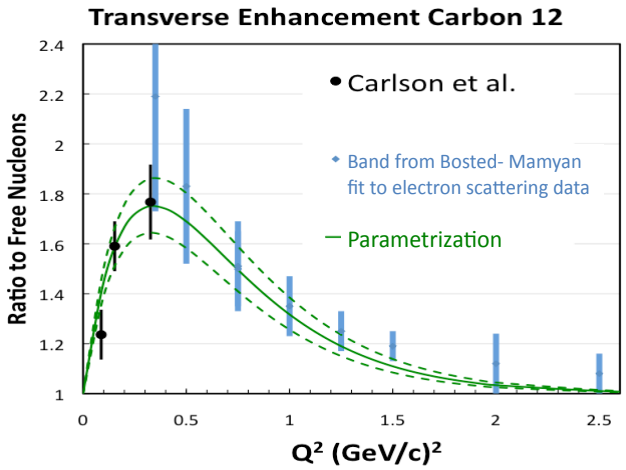

Fig. 7. The transverse enhancement ratio[14] ($\mathcal{R}_T$) as a function of Q^2. Here, $\mathcal{R}_T$ is ratio of the integrated transverse response function for QE electron scattering on nucleons bound in carbon divided by the integrated response function for independent nucleons. The black points are extracted from Carlson *et al*[16], and the blue bands are extracted from a fit[19] to QE data from the JUPITER[18] experiment (Jlab experiment E04-001). The curve is a fit to the data of the form $\mathcal{R}_T = 1 + AQ^2e^{-Q^2/B}$. The dashed lines are the upper and lower error bands (color online).

$$W_{5-Qelastic}^{\nu-vector} = \delta(\nu - \frac{Q^2}{2M})\frac{1}{2}|\mathcal{F}_V(Q^2)|^2$$

$$W_{5-Qelastic}^{\nu-axial} = \delta(\nu - \frac{Q^2}{2M})\frac{1}{2}|\mathcal{F}_A(Q^2)|^2$$

where

$$\mathcal{G}_E^V(Q^2) = G_E^p(Q^2) - G_E^n(Q^2),$$
$$\mathcal{G}_M^V(Q^2) = G_M^p(Q^2) - G_M^n(Q^2).$$

and

$$|\mathcal{F}_V(Q^2)|^2 = \frac{[\mathcal{G}_E^V(Q^2)]^2 + \tau[\mathcal{G}_M^V(Q^2)]^2}{1+\tau}.$$

Here, $G_E^p(Q^2)$, $G_E^n(Q^2)$, $G_M^p(Q^2)$ and $G_M^n(Q^2)$ are the electric and magnetic nucleon form factors, which are measured in electron scattering experiments. Note that:

$$\sigma_T^{vector} \propto \tau|\mathcal{G}_M^V(Q^2)|^2; \quad \sigma_T^{axial} \propto (1+\tau)|\mathcal{F}_A(Q^2)|^2$$

$$\sigma_L^{vector} \propto (\mathcal{G}_E^V(Q^2))^2; \quad \sigma_L^{axial} = 0$$

Therefore, for QE $\nu_\mu, \bar{\nu}_\mu$ scattering only $\mathcal{G}_M^V$ contributes to the transverse virtual boson absorption cross section.

4.2 Transverse enhancement QE scattering from nuclei

Studies of QE electron scattering on nuclear targets[16] indicate that only the longitudinal part of the QE cross section can be described in terms of a universal response function of independent nucleons bound in a nuclear potential (and free nucleon form factors). In contrast, a significant additional enhancement with respect to the model is observed in the transverse part of the QE cross section.

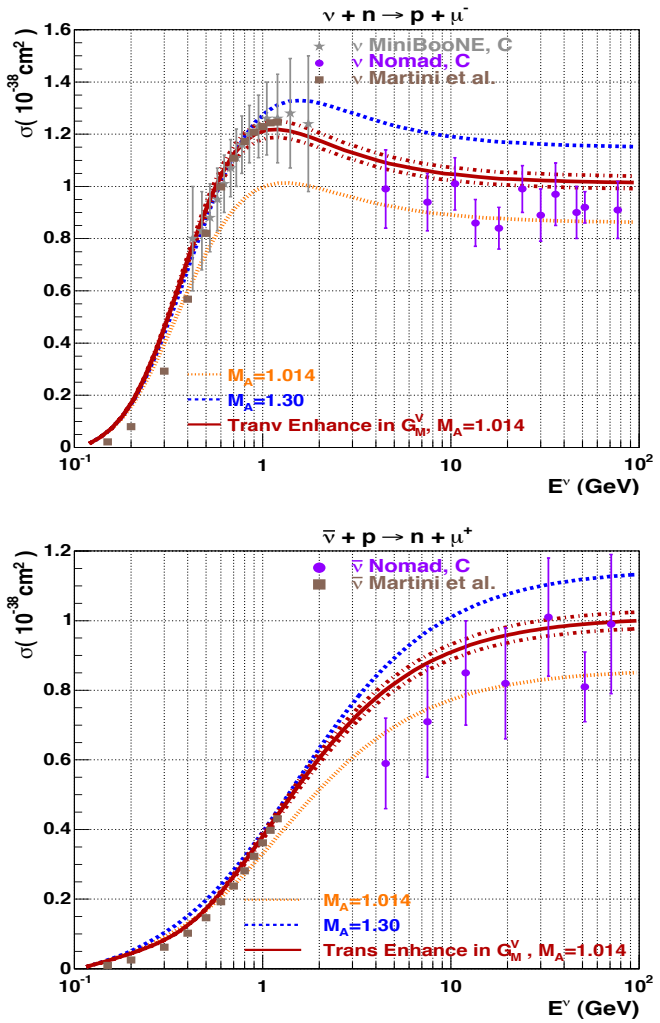

Fig. 8. Comparison of predictions for the ν_μ, $\bar{\nu}_\mu$ total QE cross section sections from the nominal TE model, the "Independent Nucleon (MA=1.014)" model, the "Larger M_A (M_A=1.3) model", and the "QE+np-nh RPA" MEC model of Martini et al.[20] The data points are the measurements of MiniBooNE[21] (gray stars) and NOMAD[22] (purple circles) (color online).

The enhancement in the transverse QE cross section has been attributed to meson exchange currents (MEC) in a nucleus. Within models of meson exchange currents the enhancement is primarily in the transverse part of the QE cross section, while the enhancement in the longitudinal QE cross section is small (in agreement with the electron scattering experimental data).

The conserved vector current hypothesis (CVC) implies that the corresponding vector structure function for the QE cross section in $\nu_\mu, \bar{\nu}_\mu$ scattering can be expressed in terms of the structure functions measured in electron scattering on nuclear targets. Therefore, there should also be a transverse enhancement in neutrino scattering. In models of meson exchange currents the enhancement in

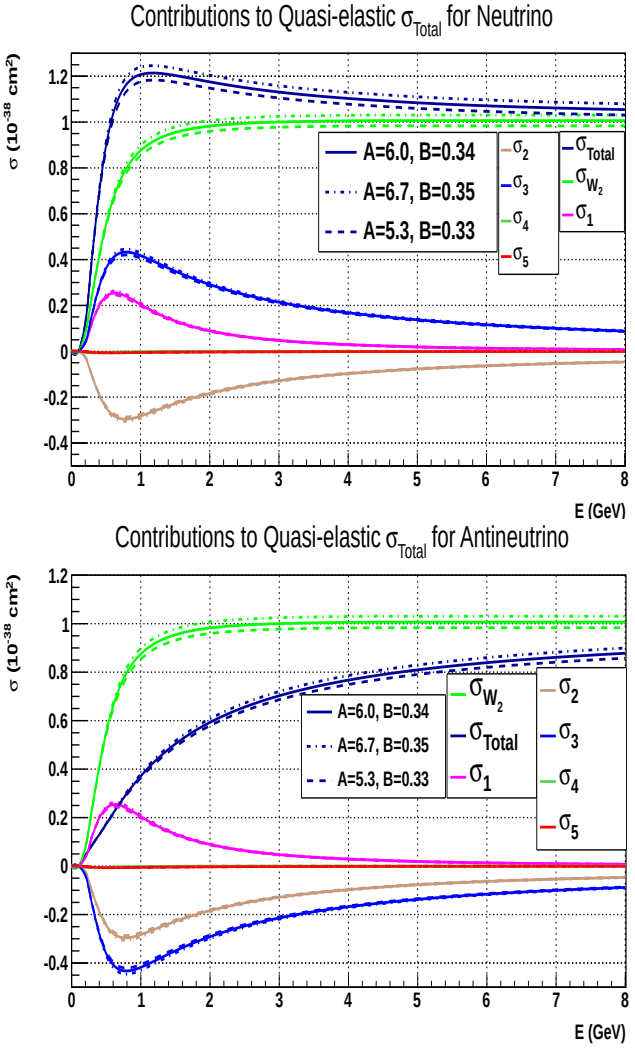

Fig. 9. Contribution of the various components (σ_{W_2}, σ_2, σ_1, σ_3, σ_4, σ_5) to the total QE cross section (a predicted by the TE model). Top panel: Neutrinos. Bottom panel: Antineutrinos (color online).

the axial part of $\nu_\mu, \bar{\nu}_\mu$ QE cross section on nuclear targets is also expected small.

The transverse enhancement observed in electron scattering is a function of both Q^2 and ν. However, a simple way to account for the integrated transverse enhancement[14] from nuclear effects is to assume that $G_M^p(Q^2)$ and $G_M^n(Q^2)$ are enhanced in a nuclear targets by factor $\sqrt{R_{TL}}$.

Bodek, Budd and Christy[14] have used electron scattering data[16,18,19] to parametrize R_{TL} as follows:

$$R_{TL} = 1 + AQ^2 e^{-Q^2/B}$$

with $A = 6.0$ and $B = 0.34$ GeV^2. The electron scattering data indicates that the transverse enhancement is maximal near Q^2=0.3 GeV^2 and is small for Q^2 greater than 1.5 GeV^2. The upper error band is given by $A = 6.7$ and $B = 0.35$ GeV^2, and the lower error band is given by $A = 5.3$ and $B = 0.33$ GeV^2.

In modeling $\nu_\mu, \bar{\nu}_\mu$ QE scattering on nuclear targets we use $BBBA2007_{25}$ parametrization[17] of the free nucleon electromagnetic form factors $G_E^p(Q^2)$, $G_E^n(Q^2)$, $G_M^p(Q^2)$ and $G_M^n(Q^2)$ (with $M_V^2 = 0.71$ GEV^2), and a dipole axial form factor with $M_A = 1.014\ GeV$. We apply the transverse enhancement correction to $G_M^p(Q^2)$ and $G_M^n(Q^2)$. We also apply Pauli blocking corrections to the differential QE cross section as parametrized by Paschos and Yu[11]. We refer to this model as the Transverse Enhancement (TE) model. This is the nominal model that is used in this paper.

We also compare calculations based on the nominal TE model to two other models. The first model is the independent nucleon model with Pauli blocking with $M_A = 1.014\ GeV$, without transverse enhancement. We refer to this model as the "Independent Nucleon (MA=1.014)" model. This model is very close to the model which is currently implemented in the GENIE Monte Carlo (the GENIE default value is $M_A = 0.99\ GeV$"). The second model is the independent nucleon model with Pauli blocking, $M_A = 1.3$ GeV, without transverse enhancement. We refer to this model as the "Larger M_A (M_A=1.3) model". We use the difference between the three models as a conservative systematic error on the flux extracted from the ν samples.

Fig. 8 shows a comparison of predictions of various model predictions for the $\nu_\mu, \bar{\nu}_\mu$ total QE cross section sections to experimental data on nuclear targets. Shown are "Independent Nucleon (MA=1.014)" model, the "Larger M_A (M_A=1.3) model", and the TE model (with upper and lower error bands). Also shown are the predictions of the "QE+np-nh RPA" MEC model of Martini et al.[20] The data points are the QE cross section measurements of MiniBooNE[21] (gray stars) and NOMAD[22] (purple circles). Note that there is an overall $\approx 10\%$ systematic error in the experimental QE cross sections because of uncertainties in the determination of the neutrino and antineutrino fluxes in each of the two experiments.

In this paper we use the error band in the transverse enhancement parameters as a lower limit on systematic error in the modeling. We use the "Independent Nucleon (MA=1.014)" and the "Larger M_A (M_A=1.3) model" as conservative upper limits on the errors in the modeling.

Fig. 9 shows the contribution of the various components (σ_{W_2}, σ_2, σ_1, σ_3, σ_4, σ_5) to the total QE cross section (as defined by Eq. 12) as a function of incident energy. These contributions are calculated using the TE model. The top panel shows the contribution of the various components for the neutrino QE cross section, and the bottom panel shows the contribution of the various components for the antineutrino QE cross section.

4.3 Neutrino and antineutrino total cross sections

The MINOS collaboration uses the criteria that the fraction of low ν events that are used for the determination of the relative neutrino flux in an energy bin should be

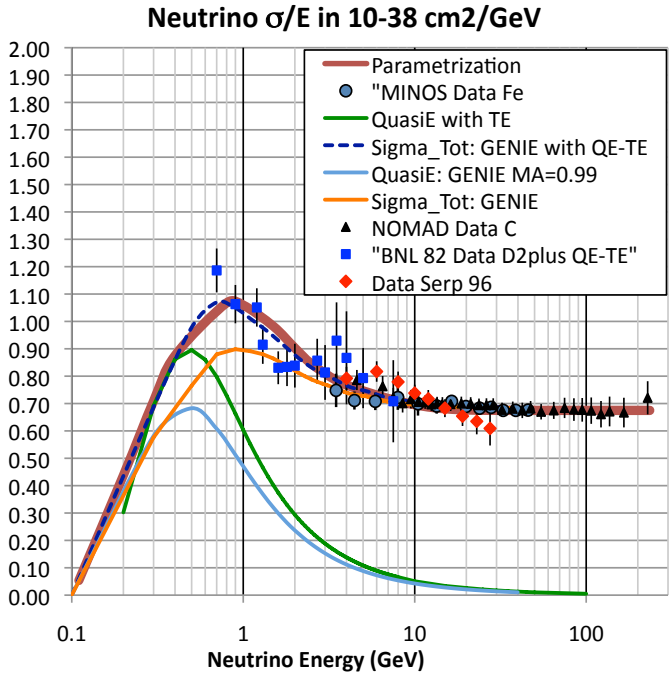

Fig. 10. The MINOS[3](iron), NOMAD[22](carbon) and Serp96[23] (aluminum) measurements of σ_{total}/E per nucleon on isoscalar nuclear targets for ν in units of $10^{-38} cm^2/GeV$ (with statistical, systematic and normalization errors combined in quadrature). We also show BNL82[24] data which was taken with a deuterium target corrected for the additional transverse enhancement in the QE contribution to the total cross section (in carbon) as discussed in the text. The orange line shows the predictions of the unmodified GENIE Monte Carlo. The QE cross section in the GENIE MC is shown as the blue line. The QE contribution calculated with the TE model is show as a green line. The dashed blue line shows the prediction of the modified GENIE MC (using the TE model QE cross section instead). The thick brown line is a parametrization described in the text (color online).

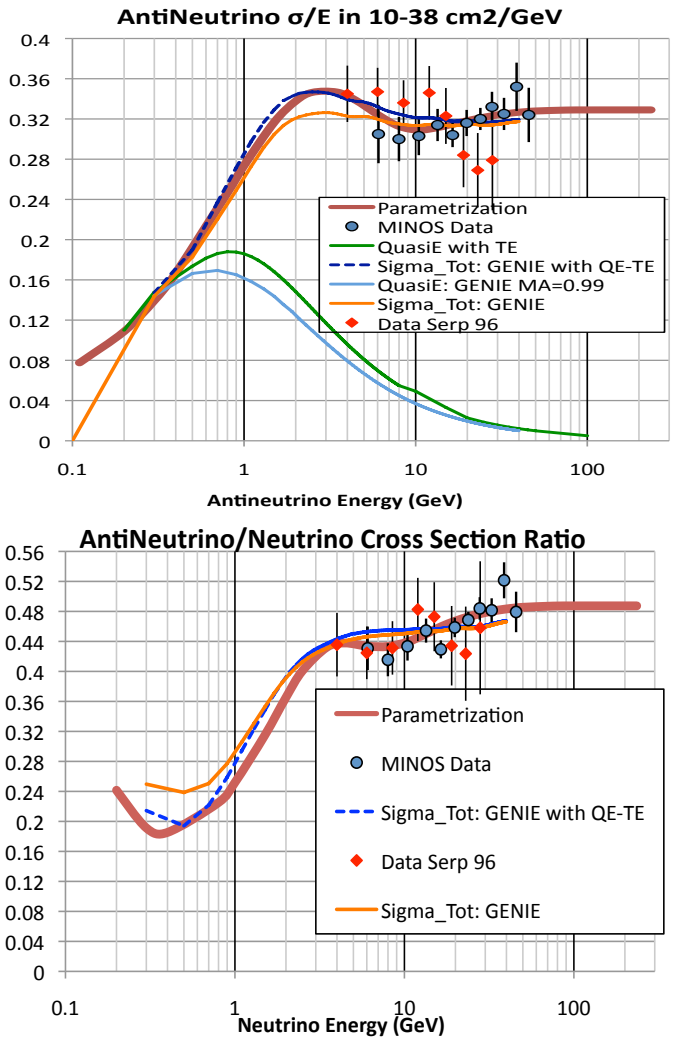

Fig. 11. Same as Fig. 10 but (a) for the antineutrino charged current cross section, (b) for the ratio of antineutrino and neutrino total cross sections (color online).

less than 60% of the total number of charged current events. In order to test for this fraction, we need to use a parametrization to estimate the energy dependence of the neutrino and antineutrino charged current total cross sections.

Fig. 10 and 11 show the ν_μ and $\bar{\nu}_\mu$ total charged current cross sections measured on isocalar nuclear targets by the MINOS[3] (iron), NOMAD[22](carbon) , and Serpukov[23] (Serp96, aluminum) experiments. The total cross sections per nucleon (divided by neutrino energy) are shown in units of $10^{-38} cm^2/GeV$ (with statistical, systematic and normalization errors combined in quadrature). The ratio of the $\bar{\nu}_\mu$ and ν_μ total charged current cross sections is shown in the bottom panel of Fig. 11. The cross sections reported by the MINOS collaboration were measured using a neutrino flux extracted from low ν samples with ν less than 1, 3, and 5 GeV.

Also shown in Fig. 10 are low energy cross sections measured by at BNL[24] (BNL82). Since the BNL82 cross sections were measured on a deuterium target we we apply a correction to account for nuclear effects. The BNL82 points shown in the figure were increased by the difference of the predictions of the TE model for the QE cross section (which is expected to describe the cross section on a heavy nuclear target) and the "Independent Nucleon (MA=1.014)" model (which is expected to describe the QE cross sections on deuterium).

The orange line shows the predictions of the GENIE Monte Carlo. The QE cross sections in the GENIE MC are a calculated using the independent nucleon model with $M_A = 0.99$ GeV. The QE contribution to the cross section from GENIE is shown as a blue line. The QE contribution calculated with the TE model is show as a green line. The curve labeled GENIE with QE-TE (shown as a dotted blue line) represent the GENIE cross section increased by the difference of the predictions of the TE model for the QE cross section (which is expected to describe the cross section on a heavy nuclear target) and the "Inde-

pendent Nucleon (MA=0.99)" model (which is currently implemented in GENIE).

In our investigation of the low ν technique, we use a parametrization to estimate the total ν_μ, $\bar{\nu}_\mu$ charged current cross sections. The parametrization, which is shown as the thick red line in Fig. 10, is given by

$$\frac{\sigma_\nu}{E_\nu} = [A + B\ e^{-E_\nu/C1} + D\ e^{-E_\nu^2/C2}](1 - Ke^{-(E_\nu - 0.1)/C3})$$

where for ν_μ we use A_ν= 0.675, B_ν= 0.12, $C1_\nu$= 9 GeV, D_ν =0.4, $C2_\nu$= 3 GeV^2, $C3_\nu$= 0.22 GeV, and K = 1.0. For $\bar{\nu}_\mu$ we use $A_{\bar{\nu}}$=0.329, $B_{\bar{\nu}}$= -0.06 and $C1_{\bar{\nu}}$=13 GeV $D_{\bar{\nu}}$= 0.09, $C2_{\bar{\nu}}$= 30 GeV^2 , $C3_\nu$= 0.8 GeV, and K = 0.8. Here, $\frac{\sigma_\nu}{E_\nu}$ is total charged current cross section per nucleon in units of $10^{-38} cm^2/GeV$.

The above form is constrained to yield the average world cross section measurements in the 30 to 50 GeV region of of 0.675 $10^{-38} cm^2/GeV$, and 0.329 $10^{-38} cm^2/GeV$ for ν_μ and $\bar{\nu}_\mu$, respectively.

We only use this parametrization to estimate the fractional contribution of low ν events to the total cross section to determine the region where it is less than 60%. When improved total cross section measurements become available (e.g. from MINERvA), this parameterization can be updated to include the new data.

4.4 Results with $\nu < 0.25$ GeV

Fig. 12 show the contribution of the various components (σ_{W_2}, σ_2, σ_1, σ_3, σ_4, σ_5) to the $\nu < 0.25$ GeV partial cross section. This sample is is dominated by QE $\nu_\mu N \to \mu^- P$ events. The partial cross section as a function of energy for neutrinos is shown in the top panel and the partial cross section for antineutrinos is shown in the bottom panel. The partial cross section (per nucleon) is calculated on a carbon target using the TE model.

The uncertainty in the relative values of the $\nu < 0.25$ GeV partial cross section as a function of energy determines the uncertainty in the determination of the relative fluxes. Here $f_C(E)$ is the ratio of the partial cross section to the value of the partial cross section at $E = \infty$.

Fig. 13(a) (top) shows the correction factor f_C for the $\nu < 0.25$ GeV sample for neutrinos as a function energy. The error bands in f_C (originating from the uncertainty in the transverse enhancement) are shown as the dotted lines, and represent the lower limit on errors. Also shown on the figure is the negative contribution from the kinematic correction f_2 (which is well known), and the contributions of f_1, f_3, f_4 and f_5. Here the contribution of f_4 and f_5 is negligible. For the case of neutrino scattering, the positive contributions of f_1 and f_3 partially cancel the negative contribution of f_2. Fig. 13(b) (bottom) shows the fractional contribution of the $\nu < 0.25$ GeV sample to the total neutrino charged current cross section. This fraction is less than 60% for ν_μ energies above 0.70 GeV.

Fig. 14(a) (top) shows the correction factor f_C for the $\nu < 0.25$ GeV sample for antineutrinos as a function energy. The error bands in f_C (originating from the uncertainty in the transverse enhancement) are shown as the

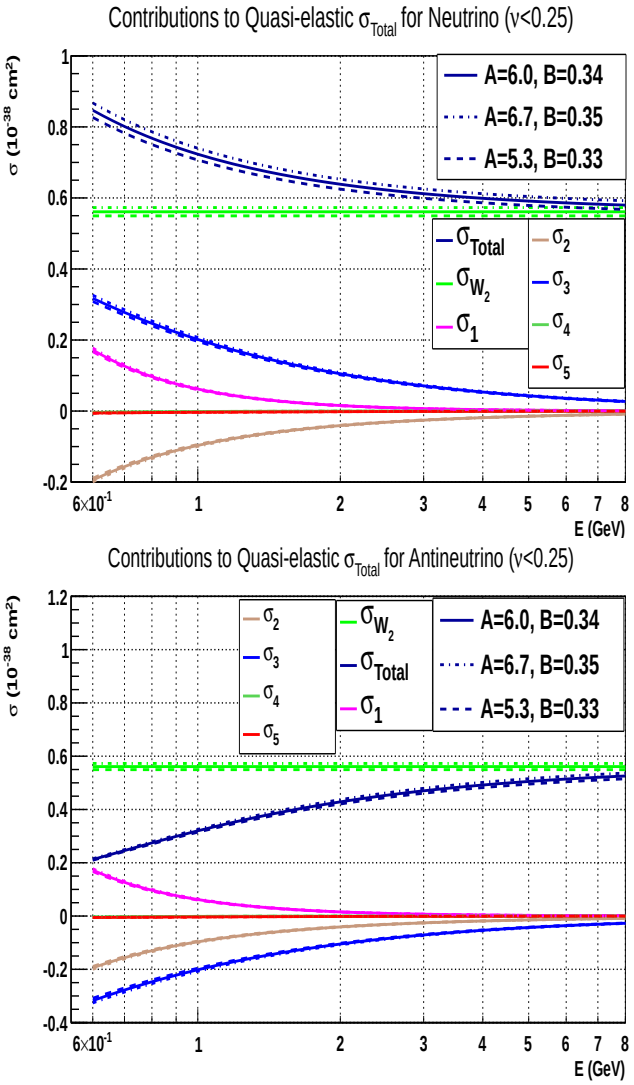

Fig. 12. Contribution of the various components (σ_{W_2}, σ_2, σ_1, σ_3, σ_4, σ_5) to the $\nu < 0.25$ GeV partial charged current cross section. This sample is is dominated by QE $\nu_\mu N \to \mu^- P$ events. Top panel: Neutrinos. Bottom panel: Antineutrinos (color online).

dotted lines, and represent the lower limit on errors. Also shown on the figure is the negative contribution from the kinematic correction f_2 (which is well known), and the contributions of f_1, f_3, f_4 and f_5. Here the contribution of f_4 and f_5 is negligible. For the case of antineutrino scattering f_3 changes sign, and both f_2 and f_3 are negative. Fig. 14(b) (bottom) shows the fractional contribution of the $\nu < 0.25$ GeV sample to the total antineutrino charged current cross section. This fraction is less than 60% for $\bar{\nu}_\mu$ energies above 1.0 GeV.

4.4.1 Uncertainty in the f_C correction factors

It has been traditional to use the value and error in the effective M_A extracted from neutrino scattering data as an

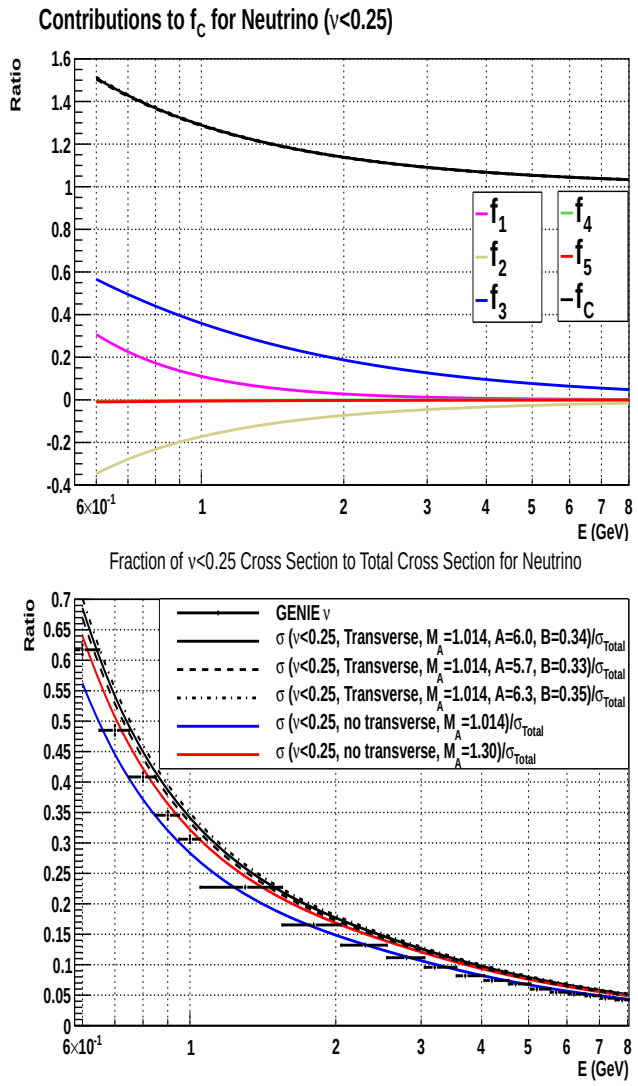

Fig. 13. The $\nu < 0.25$ GeV sample for ν_μ scattering on carbon. This sample is dominated by QE $\nu_\mu N \to \mu^- P$ events. Top panel: The total correction factor f_C (black line), the contribution of the kinematic correction to $\mathcal{W}_2$ (f_2) (yellow line), the contributions from $\mathcal{W}_1$ (f_1) (pink line), the contribution from $\mathcal{W}_3$ (f_3) (blue line), and the very small contributions of $\mathcal{W}_4$ (f_4), and $\mathcal{W}_5$ (f_5). Bottom panel: The fractional contribution of $\nu < 0.25$ GeV events to the total ν_μ charged current cross section. The fraction is less than 60% for ν_μ energies above 0.7 GeV (color online).

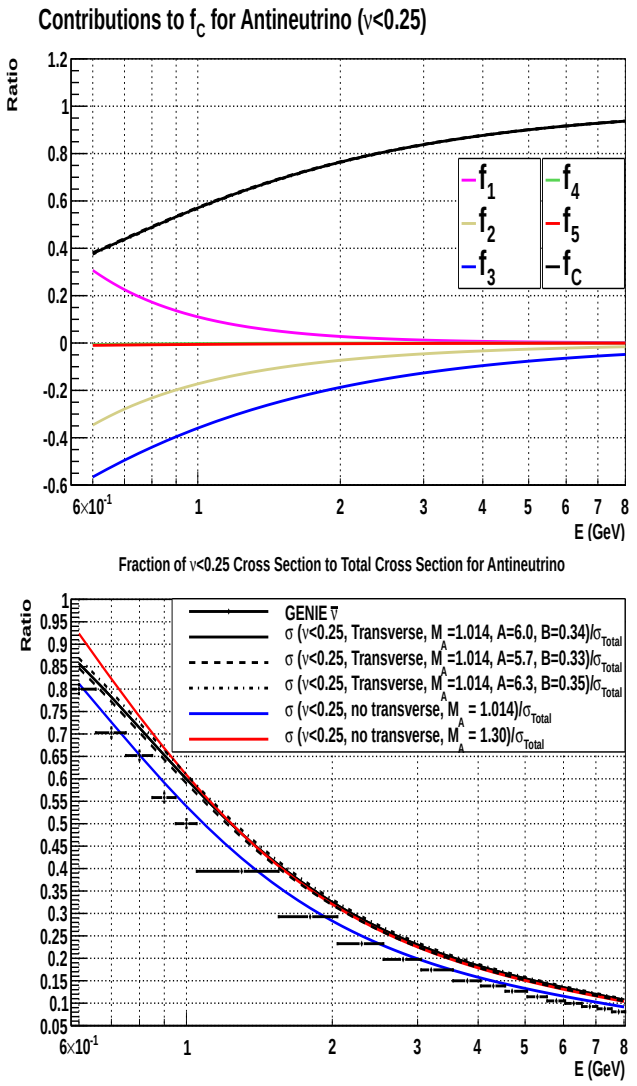

Fig. 14. The $\nu < 0.25$ GeV sample for $\bar{\nu}_\mu$ scattering on carbon. This sample is dominated by QE $\bar{\nu}_\mu P \to \mu^+ N$ events. Top panel: The total correction factor f_C (black line), the contribution of the kinematic correction to $\mathcal{W}_2$ (f_2) (yellow line), the contributions from $\mathcal{W}_1$ (f_1) (pink line), the contribution from $\mathcal{W}_3$ (f_3) (blue line), and the very small contributions of $\mathcal{W}_4$ (f_4), and $\mathcal{W}_5$ (f_5). Bottom panel: The fractional contribution of $\nu < 0.25$ GeV events to the $\bar{\nu}_\mu$ total charged current cross section. The fraction is less than 60% for $\bar{\nu}_\mu$ energies above 1.0 GeV (color online).

estimate of various uncertainties. Typically, the difference between results with $M_A = 1.014$ GeV and $M_A = 1.3$ GeV are used an upper limit on the error.

We find that the values of the f_C correction factor are insensitive to M_A. This is because at small Q^2, both ratios f_1, and f_3 are insensitive to M_A. Specifically, both

$$\frac{\mathcal{W}_1^{QE}}{\mathcal{W}_2^{QE}} = \frac{(1+\tau)|\mathcal{F}_A(Q^2)|^2 + \tau|\mathcal{G}_M^V(Q^2)|^2}{|\mathcal{F}_A(Q^2)|^2 + [\mathcal{F}_V(Q^2)]^2}$$

$$\frac{\mathcal{W}_3^{QE}}{\mathcal{W}_2^{QE}} = \frac{|2\mathcal{G}_M^V(Q^2)\mathcal{F}_A(Q^2)|}{|\mathcal{F}_A(Q^2)|^2 + [\mathcal{F}_V(Q^2)]^2},$$

are insensitive to M_A because the change in F_A at small Q^2 is small. Since f_C is insensitive to large variations in M_A one may naively surmise that the error in f_C is small.

However, we find that the difference between the values f_C calculated with and without transverse enhancement is larger than the error estimate extracted from the uncertainty in M_A. This is because $\frac{\mathcal{W}_3^{QE}}{\mathcal{W}_2^{QE}}$ is sensitive to $\mathcal{G}_M^V(Q^2)$, which depends on the magnitude of the transverse enhancement at small Q^2.

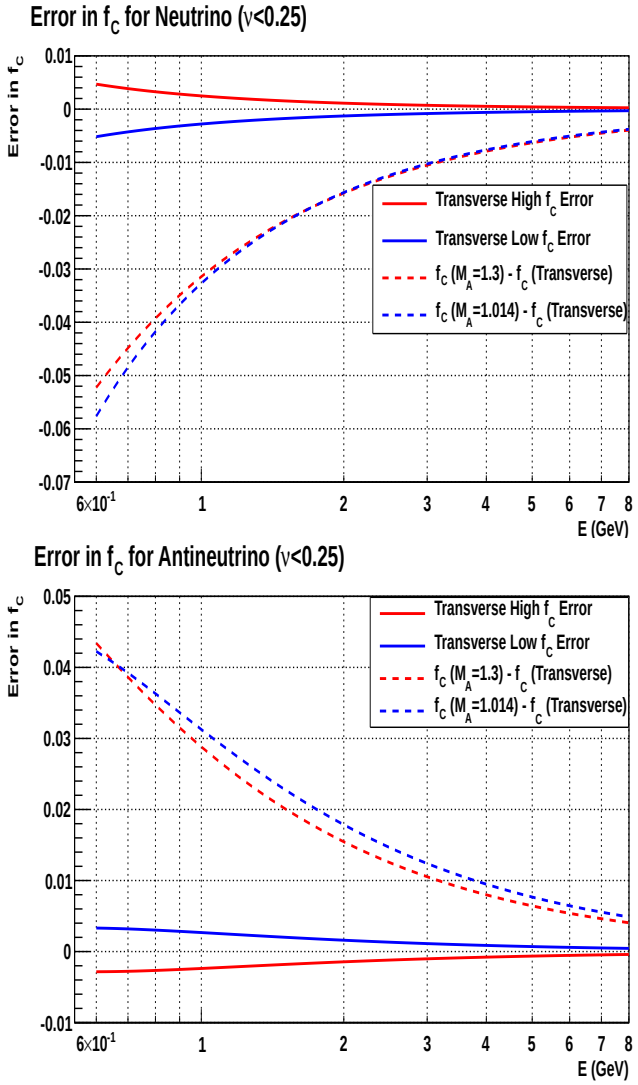

Fig. 15. The error band in the correction factor f_C for $\nu <$ 0.25 GeV. Top panel: Neutrinos. Bottom panel: Antineutrinos (color online).

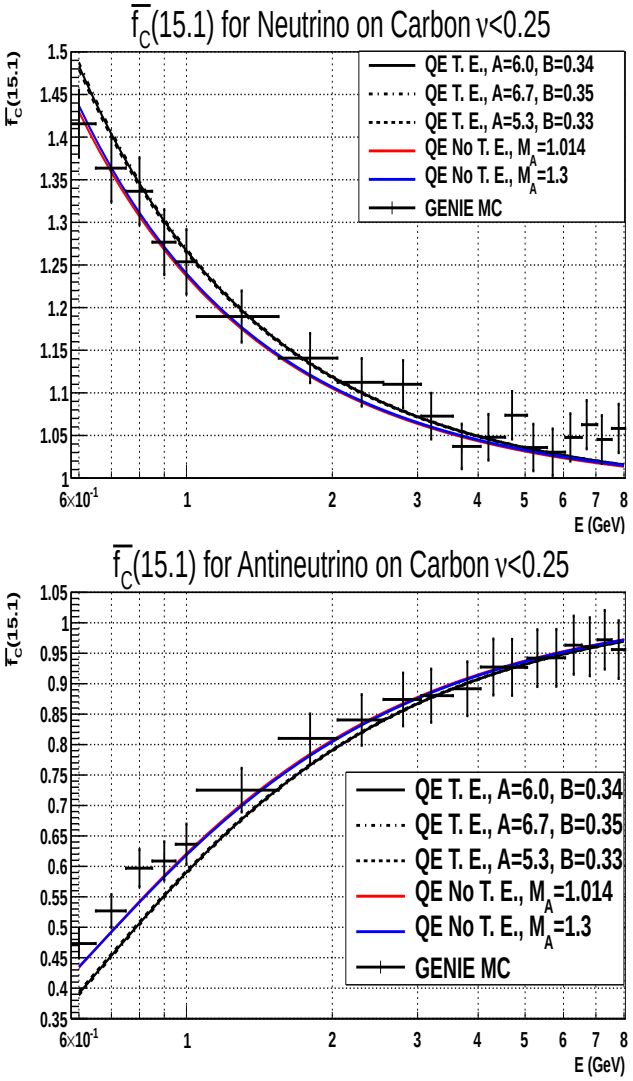

Fig. 16. Comparisons of our calculated values of the normalized $\bar{f}_{C:\nu<0.25}(15.1)(E)$ ($=\bar{f}_C(15.1)$ for $\nu <$ 0.25 GeV) to values from the GENIE MC. The values calculated with the nominal TE model for QE scattering (M_A = 1.014 GeV) are shown in black. The values calculated assuming no transverse enhancement and M_A = 1.014 GeV are shown in red. The GENIE prediction (which has no transverse enhancement and uses M_A = 0.99 GeV) is close to the red curve as expected. As discussed in the text, the values for M_A = 1.014 GeV (red line) and M_A = 1.3 GeV (blue line) are very close to each other (color online).

Fig. 15 shows the errors in f_C from the uncertainty in the TE parameters. The error originating from uncertainties in the TE parameters is also very small (less than 0.005).

We obtain a more conservative estimate of the systematic error from uncertainties in the modeling the QE cross section by taking the difference between f_C calculated with and without transverse enhancement. At the lowest energy of 0.7 GeV, this difference is -0.05 for ν_μ. Since at 0.7 GeV $f_C^\nu \approx 1.3$ this corresponds to a maximum error in the determination of the ν_μ flux of 3.8%.

For $\bar{\nu}_\mu$ the difference between f_C calculated with and without transverse enhancement at an energy of 1.0 GeV is +0.03. Since at 1.0 GeV $f_C^{\bar{\nu}} \approx 0.6$ this corresponds a maximum error in the determination of the $\bar{\nu}_\mu$ flux of 5%.

These differences can be used as upper limits on the model uncertainties in f_C. If one takes the average of all the models, a conservative upper limit of the model uncertainty in the relative flux extracted from the $\nu <$ 0.25 GeV sample is 1.9% for ν_μ energies above 0.7 GeV and 2.5% for $\bar{\nu}_\mu$ energies above 1.0 GeV.

A study of the Q^2 distributions of QE events in MINERvA can be used to constrain the Q^2 dependence of the QE differential cross sections and thus reduce the model dependence in the determination of the relative flux to a negligible level (and also extend the technique to lower energies).

4.5 Comparison to GENIE and $\bar{f}_{C:\nu<0.25}$(15.1 GeV)

We have used a sample of events generated by the GENIE Monte Carlo. Our studies are done at the generated level and therefore do not depend on the detector parameters or energy resolutions of any specific experiment.

We extract the energy dependence of the $\nu < 0.25$ GeV cross section from the GENIE MC sample using the following expression:

$$\sigma^{MC}_{\nu<0.25}(E) = \frac{N^{MC}_{\nu<0.25}(E)}{N^{MC}_{QE}(E)} \times \sigma^{MC}_{QE}(E)$$

where the superscript MC refers to events generated by the GENIE Monte Carlo.

Here, $N^{MC}(E)$ is the number of events generated by the Monte Caro with neutrino energy E, and $N^{MC}_{\nu<0.25}(E)$ is the subset of these events with $\nu < 0.25$ GeV.

As mentioned earlier, we propose that the neutrino cross sections at low energy be measured relative to the neutrino cross section at 15.1 GeV. For any cross section model we can define the normalized quantity $\bar{f}_{C:\nu<0.25}$(15.1 GeV) as:

$$\bar{f}_{C:\nu<0.25}(15.1)(E) = \sigma_{\nu<0.25}(E)/\sigma_{\nu<0.25}(E = 15.1\ GeV)$$

which is equivalent to

$$\bar{f}_{C:\nu<0.25}(15.1)(E) = f_{C:\nu<0.25}(E)/f_{C:\nu<0.25}(E = 15.1\,GeV)$$

We compare the values of $\bar{f}_{C:\nu<0.25}(15.1)(E)$ predicted by the GENIE MC to our calculations.

For all of the models, the value of $f_{C:\nu<0.25}$(E=15.1 GeV)= (for ν) and 0.995 (for $\bar{\nu}$). These values can be used to convert between $\bar{f}_{C:\nu<0.25}(E)$ and $f_{C:\nu<0.25}(E)$.

Comparisons of our calculated values of the normalized $\bar{f}_{C:\nu<0.25}(15.1)(E)$ to values from the GENIE MC are shown in Fig. 16. The top panel shows the comparison for neutrinos and the bottom panel shows the comparison for antineutrinos. Our calculation for the TE model is shown in black. Our calculation assuming no transverse enhancement and $M_A = 1.014$ GeV is shown in red. As mentioned earlier, the values for $M_A = 1.014$ GeV (red line) and $M_A = 1.3$ GeV (blue line) are very close to each other. The GENIE prediction (which has no transverse enhancement and uses $M_A = 0.99$ GeV) is close to the red curve as expected.

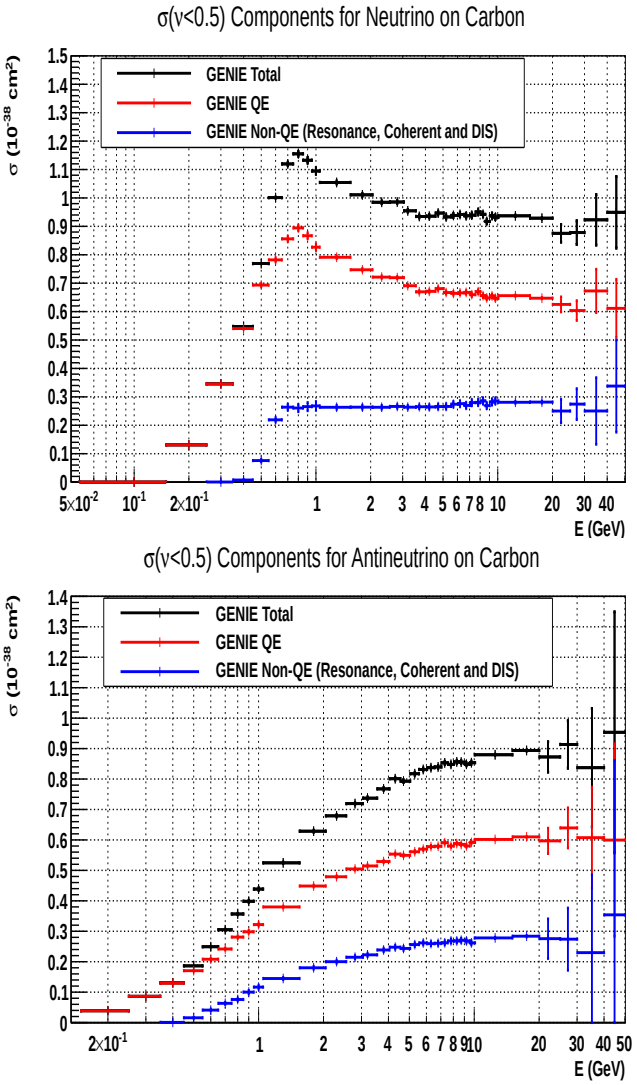

Fig. 17. The $\nu < 0.5$ GeV partial charged current cross section as a function of energy from the GENIE Monte Carlo. The QE contribution is shown in red, the contribution from pion production process (Δ, inelastic and coherent pion production) is shown in blue, and the total $\nu < 0.5$ GeV partial cross section is shown in black. The $\nu < 0.5$ GeV partial cross section for ν_μ is shown in the top panel, and the $\nu < 0.5$ GeV partial cross section for $\bar{\nu}_\mu$ is shown in the bottom panel. About 2/3 of the $\nu < 0.5$ GeV events are QE and 1/3 are from pion production production processes (color online).

5 Using low ν events with $\nu < 0.5$ GeV

The $\nu < 0.5$ GeV samples for ν_μ and $\bar{\nu}_\mu$ scattering are also dominated by QE events, but include a significant fraction (about 1/3) of events in which a single pion is produced in the final state. As seen in Fig. 3, the $\nu < 0.5$ GeV samples are composed of QE events with $Q^2 < 0.9$ GeV^2, and $\Delta(1232)$ events with $Q^2 < 0.3$ GeV^2.

Fig. 17 shows the $\nu < 0.5$ GeV partial charged current cross sections as a function of energy. The partial cross sections extracted from from the GENIE Monte Carlo are shown as black points with MC statistical errors. The $\nu <$ 0.5 GeV partial cross section for ν_μ scattering is shown on the top panel, and the $\nu < 0.5$ GeV partial cross section for $\bar{\nu}_\mu$ scattering is shown on the bottom panel. The QE contribution to the $\nu < 0.5$ GeV partial cross section is shown in red, and the contribution from pion production processes (Δ, inelastic and coherent pion production) is shown in blue.

As seen in Fig. 17, the pion production contribution to the $\nu < 0.5$ GeV partial cross section is relatively constant with energy, while the QE contribution has some energy dependence. Therefore, the energy dependence of the sum

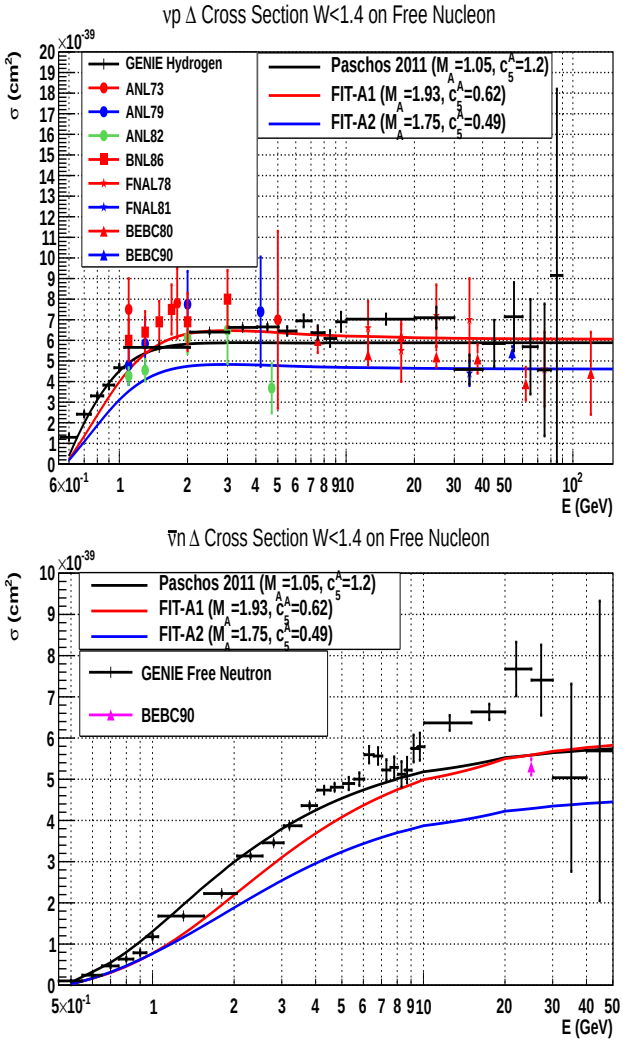

Fig. 18. $\nu_\mu P \to \mu^- \Delta^{++}$ (top panel) and $\bar{\nu}_\mu N \to \mu^+ \Delta^-$ (bottom panel) cross sections (for $W < 1.4$ GeV) measured on free nucleons (H and D), compared to predictions from the GENIE MC (black points with errors). The structure functions (form factors) for these two processes are the same. The free nucleon cross sections are expected to be higher than the corresponding cross sections on nuclear targets which are shown in Fig. 19 (because of Pauli suppression and final state interactions). The black curve labeled Paschos-2011(M_A^Δ=1.05, $C_5^A = 1.2$), the red curve labeled FIT-A1 (M_A=1.93, $C_5^A = 0.62$) and the blue curve labeled FIT-A2 (M_A=1.75, $C_5^A = 0.49$) represent three parametrization that conservatively span the available data on H,D and nuclear targets. The cross sections predicted by GENIE on free nucleons are near the upper bound of our three parametizations (color online).

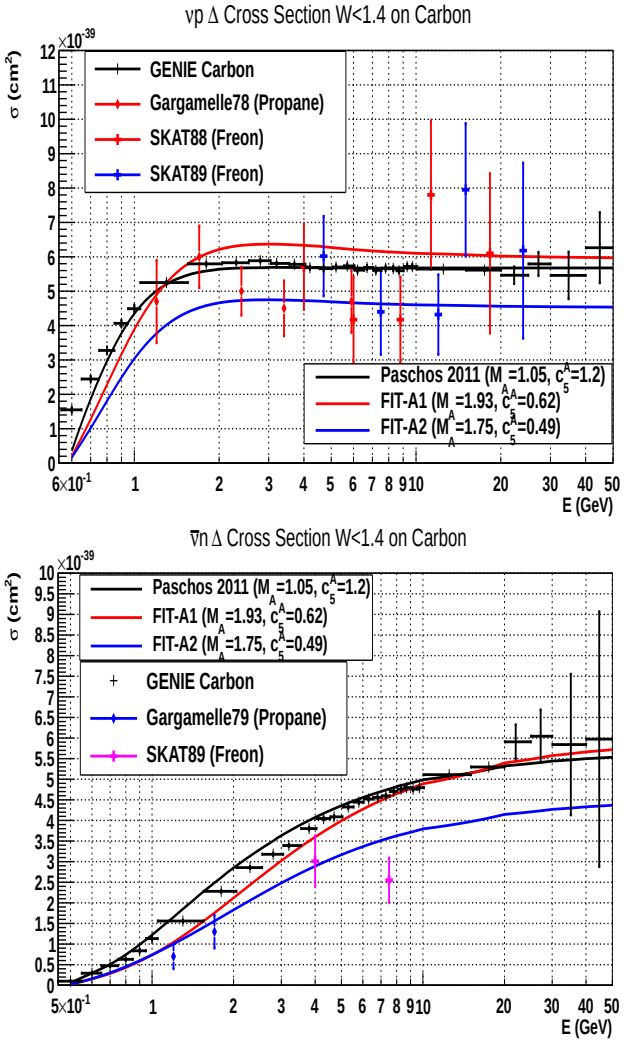

Fig. 19. $\nu_\mu P \to \mu^- \Delta^{++}$ (top panel) and $\bar{\nu}_\mu N \to \mu^+ \Delta^-$ (bottom panel) cross sections (for $W < 1.4$ GeV)) measured on nuclear targets, compared to predictions from the GENIE MC (black points with errors). The structure functions (form factors) for these two processes are same. The cross sections on nuclear targets are expected to be somewhat smaller than the corresponding cross sections for free nucleons which are shown in Fig. 18 (because of Pauli suppression and final state interactions). The black curve labeled Paschos-2011(M_A^Δ=1.05, $C_5^A = 1.2$), the red curve labeled FIT-A1 (M_A=1.93, $C_5^A = 0.62$) and the blue curve labeled FIT-A2 (M_A=1.75, $C_5^A = 0.49$) (all include Pauli suppression) represent three parametrization that conservatively span the available data on the production of Δ^{++} and Δ^- on H,D and nuclear targets. The cross sections predicted by GENIE on nuclear targets are near the upper bound of our three parametizations (color online).

of the two contributions to the $\nu < 0.5$ GeV partial cross section requires modeling of the relative magnitude of QE and pion production processes (specifically at low Q^2).

As shown in Fig. 18 and 19, the consistency among the experimental measurements of pion production cross sections in the region of the $\Delta(1232)$ resonance is of order 20% (depending on the neutrino energy and the nuclear target). We use this variation to get an estimate of the model uncertainty in the determination of the neutrino flux from the $\nu < 0.5$ GeV samples. This uncertainty can be greatly reduced when more precise measurements of the QE and pion production cross sections become available (e.g. from MINERvA).

6 Pion production with $W < 1.4$ GeV

The antineutrino structure functions are related to the neutrino structure functions by the following relationship.

$$\begin{aligned} \mathcal{F}_i^{\bar{\nu}n} &= \mathcal{F}_i^{\nu p} \\ \mathcal{F}_i^{\bar{\nu}p} &= \mathcal{F}_i^{\nu n} \end{aligned} \tag{14}$$

6.1 $\nu_\mu P \to \mu^- \Delta^{++}$ and $\bar{\nu}_\mu N \to \mu^+ \Delta^-$ (FIT-A)

We define the cross section for $\nu_\mu P \to \mu^- \Delta^{++}$ as the integrated cross section for $W < 1.4$ GeV for the following single final state:

$$\nu_\mu P \to \mu^- P \pi^+$$

We define the cross section for $\bar{\nu}_\mu N \to \mu^+ \Delta^-$ as the integrated cross section for $W < 1.4$ GeV for the following single final state:

$$\bar{\nu}_\mu N \to \mu^+ N \pi^-$$

Therefore, our definition includes the sum of the contributions of the resonant cross section and the non-resonant continuum.

The structure functions (form factors) for the reactions $\nu_\mu P \to \mu^- \Delta^{++}$ and $\bar{\nu}_\mu N \to \mu^+ \Delta^-$ defined above are the same (except that for antineutrinos the structure function W_3 changes sign). It has been experimentally determined[32] that $\nu_\mu P$ cross section for $W < 1.4$ GeV is dominated by the resonant Δ^{++} production process. Similarly, the $W < 1.4$ GeV cross section for $\bar{\nu}_\mu N$ is dominated by the resonant Δ^- production process.

We parametrize the Δ^{++} and Δ^- production cross sections in terms of form factors as given by Paschos and Lalakulich[10], with the form factors of Paschos and D. Schalla[10]. In order to obtain predictions for the $W < 1.4$ GeV region, we divide all theoretical Δ production cross sections by a factor of 1.2 (because 20% of the resonant cross section is above $W = 1.4$ GeV). We vary two of the parameters in the model, specifically M_A^Δ and C_5^A to obtain a band that span the experimental data. We extract M_A^Δ from the measured Q^2 distributions and use C_5^A to set the overall normalization.

The top panel in Fig. 18 shows a summary of cross section measurements for $\nu_\mu P \to \mu^- \Delta^{++}$ on free nucleons (hydrogen or deuterium targets.) Shown are bubble chamber measurements at low energy from Argonne (ANL73[25], ANL79[26], ANL82[27]) and measurement at low energy from Brookhaven (BNL86[28]). Also shown are measurements at higher energies from the Fermilab bubble chamber (FNAL78[29], FNAL81[30]) and high energy data from CERN (BEBC80[31], BEBC80[32]). The bottom panel in Fig. 18 show the BEBC90[32] cross section measurements for $\bar{\nu}_\mu N \to \mu^+ \Delta^-$ on free nucleons (deuterium target). The predictions from the GENIE MC on free nucleons (shown as black points with MC statistical errors) are near the upper bound of our three parametrizations.

The black curve labeled Paschos-2011 (M_A^Δ=1.05, C_5^A = 1.2) uses the original values of M_A^Δ and C_5^A from the paper[10] by Paschos and Lalakulich. These values were obtained from fits to cross sections and Q^2 distributions measured at low energies at Brookhaven and Argonne. The red curve labeled FIT-A1 (M_A^Δ=1.93, $C_5^A = 0.62$) is derived from a fit to the cross sections and Q^2 distribution of the higher energy BEBC90[32] data for $\bar{\nu}_\mu N \to \mu^+ \Delta^-$. The blue curve labeled FIT-A2 (M_A^Δ=1.75, $C_5^A = 0.49$) is derived from a fit to the cross sections and Q^2 distribution of the higher energy BEBC90[32] data for $\nu_\mu P \to \mu^- \Delta^{++}$.

The top panel in Fig. 19 shows a summary of cross section measurements for $\nu_\mu P \to \mu^- \Delta^{++}$ data on nuclear targets. Shown are the measurements of Gargamelle78[33] (Propane), SKAT88[34] (Freon), and SKAT89[35] (Freon). The bottom panel shows measurements of $\bar{\nu}_\mu N \to \mu^+ \Delta^-$ cross sections on nuclear targets from Gargamelle78[36] (Propane) and SKAT89[35] (Freon).

Aside from Pauli suppression and final state interaction, the structure functions (form factors) for the processes in Fig. 18 and Fig. 19 are the same. The black (Paschos-2011), red (FIT-A1) and blue (FIT-A2) curves shown in the figures use the free nucleon form factors (but include the Pauli suppression for the case of nuclear targets). The calculations do not include the effect of final state interaction for the nuclear targets. The three curves (Paschos-2011, FIT-A1 and FIT-A2) conservatively span all the available Δ^{++} and Δ^- production cross sections on hydrogen, deuterium and nuclear targets, as shown in Fig. 18 and 19. The cross sections for the production of Δ^{++} and Δ^- on nuclear targets predicted by GENIE are near the upper bound of our three parametrizations.

Additional details are given in the Appendix.

6.2 $\nu_\mu N \to \mu^- \Delta^+$ and $\bar{\nu}_\mu P \to \mu^+ \Delta^0$ (FIT-B)

We define the cross section for $\nu_\mu N \to \mu^- \Delta^+$ as the sum of the integrated cross sections for $W < 1.4$ GeV for the following two final states:

$$\nu_\mu P \to \mu^- N \pi^+$$

$$\nu_\mu P \to \mu^- P \pi^0$$

We define the cross section for $\bar{\nu}_\mu P \to \mu^+ \Delta^0$ as the sum of the integrated cross sections for $W < 1.4$ GeV for the following two final states:

$$\bar{\nu}_\mu N \to \mu^+ P \pi^-$$

$$\bar{\nu}_\mu N \to \mu^+ N \pi^0$$

Therefore, our definition includes the sum of the contributions of the resonant cross section and non-resonant continuum.

The structure functions (form factors) for the reactions $\nu_\mu N \to \mu^- \Delta^+$ and $\bar{\nu}_\mu P \to \mu^+ \Delta^0$ defined above are the same (except that for antineutrinos the structure function W_3 changes sign). Because of Clebsch-Gordan coefficients[10] the form factors for $\nu_\mu N$ resonant production

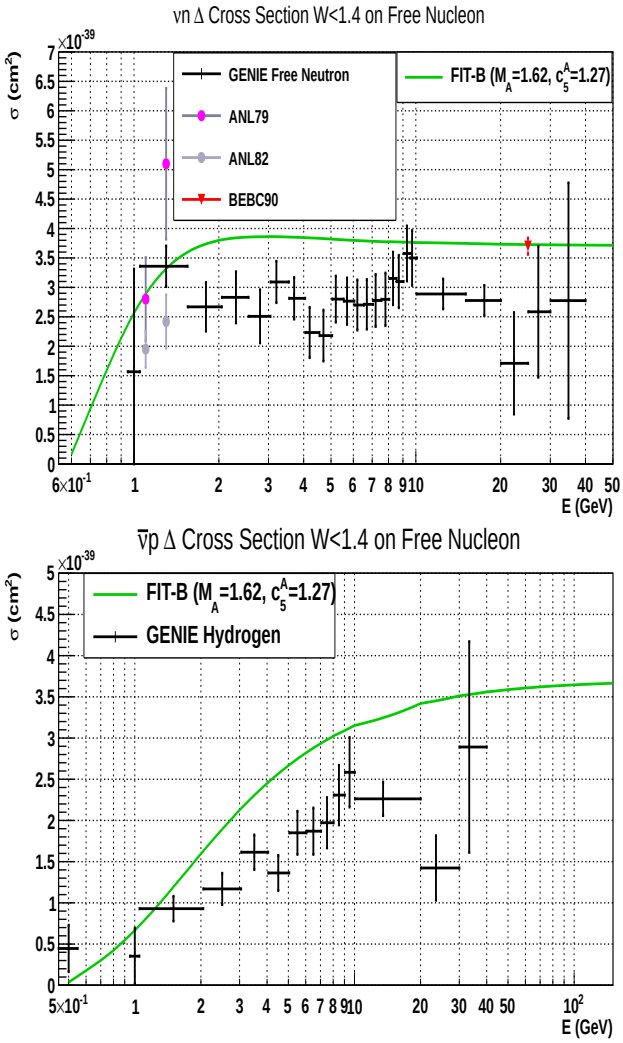

Fig. 20. $\nu_\mu N \to \mu^- \Delta^+$ (top panel) and $\bar{\nu}_\mu P \to \mu^+ \Delta^0$ (bottom panel) cross sections ($W < 1.4\,GeV$) measured on free nucleons (H or D). The predictions from the GENIE MC are shown as black points with errors. The structure functions (form factors) for these two processes are expected to be the same. The cross sections on free nucleons are expected to be higher than the cross sections on nuclear targets (which are shown in Fig. 21). The green curve labeled FIT-B (M_A^Δ=1.62, C_5^A = 1.27) provides a parametrization of structure functions which describe the for the production of production of Δ^+ and Δ^0 free nucleon data. The GENIE MC cross section for Δ^+ and Δ^0 production on free nucleons are lower than the fit (color online).

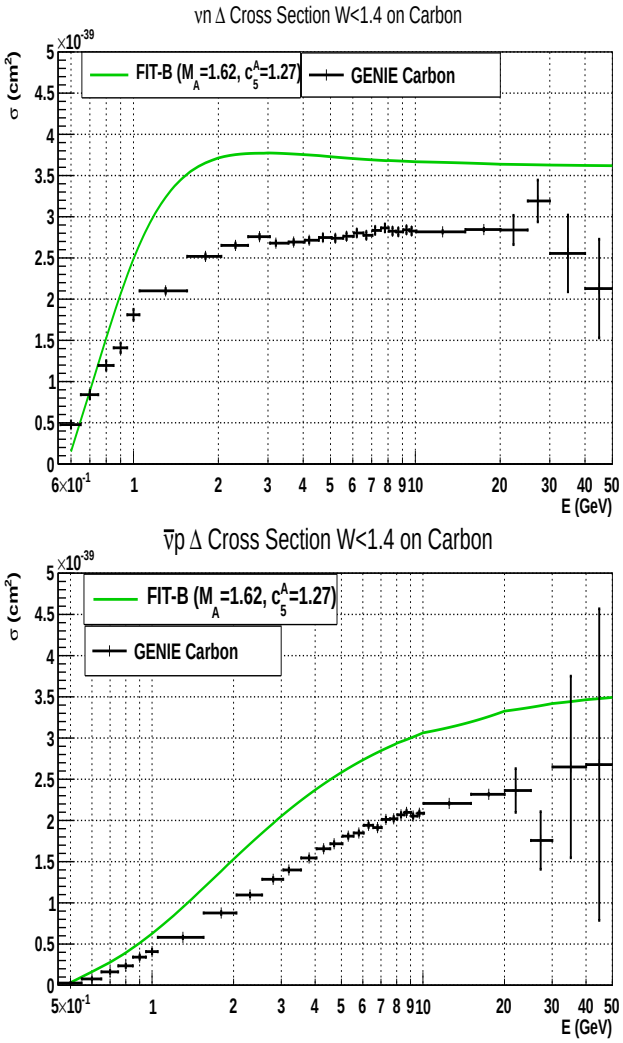

Fig. 21. $\nu_\mu N \to \mu^- \Delta^+$ (top panel) and $\bar{\nu}_\mu P \to \mu^+ \Delta^0$ (bottom panel) ($W < 1.4$ GeV) cross sections on nuclear targets predicted by FIT-B (M_A^Δ=1.62, C_5^A = 1.27). The fit, which is shown as the green line, is compared to predictions from the GENIE MC, which are shown black points with MC statistical errors. The fit uses form factors obtained from a parametrization data on free nucleons, and includes the effect of Pauli suppression (but not final state interaction). The structure functions (form factors) for these two processes are expected to be the same, and the cross sections somewhat smaller than the cross sections for free nucleons (which are shown in Fig. 20), because of Pauli suppression and final state interactions. The GENIE MC cross section for Δ^+ and Δ^0 on nuclear targets are lower than the fit (color online).

of the Δ^+ are equal to the form factors for the $\nu_\mu N$ times $1/\sqrt{(3)}$. This implies that the resonant cross section for Δ^+ production in $\nu_\mu N$ collisions is a third of the resonant cross section for Δ^{++} production in $\nu_\mu P$ collisions. Similarly, the resonant cross section for Δ^0 production in $\bar{\nu}_\mu P$ collisions is a third of the cross section for resonant Δ^- in $\bar{\nu}_\mu N$ collisions.

However, unlike the case for $\nu_\mu P$ (Δ^{++}) and $\bar{\nu}_\mu N$ (Δ^-), where the cross sections are dominated by the resonant process, there is a significant contribution from the non-resonant continuum to the $W < 1.4$ GeV cross section in $\nu_\mu N$ and $\bar{\nu}_\mu P$ collisions.

The top panel of Fig. 20 shows the $\nu_\mu N \to \mu^- \Delta^+$ cross sections ($W < 1.4\ GeV$) measured on free nucleons (deuterium). Shown are measurements from ANL79[26], ANL82[27], and BEBC90[32]. The predictions from the GENIE MC are shown as black points with MC statistical errors. In order to describe the data (which has a large non-resonant contribution) we changed the parame-

ters in the Paschos and Lalakulich[10] resonance model to fit the observed Q^2 distribution and total $W < 1.4$ GeV cross sections. The green curve labeled FIT-B (M_A^{Δ}=1.62, $C_5^A = 1.27$) is derived from a fit to the $W < 1.4$ GeV cross sections and Q^2 distribution of the BEBC90[32] data for $\nu_\mu N \to \mu^- \Delta^+$. This curve provides a parametrization which describe the experimental data for the production of Δ^+ (with neutrinos) and Δ^0 (for antineutrinos) on free nucleons. The GENIE MC cross sections for the production of Δ^+ on free nucleons are lower than the fit.

The structure functions (form factors) for the reactions $\nu_\mu N \to \mu^- \Delta^+$ and $\bar{\nu}_\mu P \to \mu^+ \Delta^0$ ($W < 1.4\ GeV$) are are same. The bottom panel of Fig. 20 shows a comparison of the predictions of FIT-B (M_A^{Δ}=1.62, $C_5^A = 1.27$) (green curve) for the $\bar{\nu}_\mu P \to \mu^+ \Delta^0$ cross sections on free nucleons compared to the predictions from the GENIE MC which are shown as black points with MC statistical errors. The GENIE MC cross sections for the production of Δ^0 on free nucleons are lower than the fit.

Fig. 20 shows the prediction of FIT-B (M_A^{Δ}=1.62, $C_5^A = 1.27$) (green curve) for the $\nu_\mu N \to \mu^- \Delta^+$ (top panel) and $\bar{\nu}_\mu P \to \mu^+ \Delta^0$ (bottom panel) $W < 1.4$ GeV cross sections on nuclear targets compared to predictions from the GENIE MC (black points with MC statistical errors). The cross sections on nuclear targets are expected to be somewhat lower than the cross sections on free nucleons (which are shown in Fig. 20). Here, FIT-B includes the effect of Pauli suppression (but not final state interaction). The GENIE MC cross sections for the production of Δ^+ and Δ^0 on nuclear targets are lower than the fit.

Additional details are given in the Appendix.

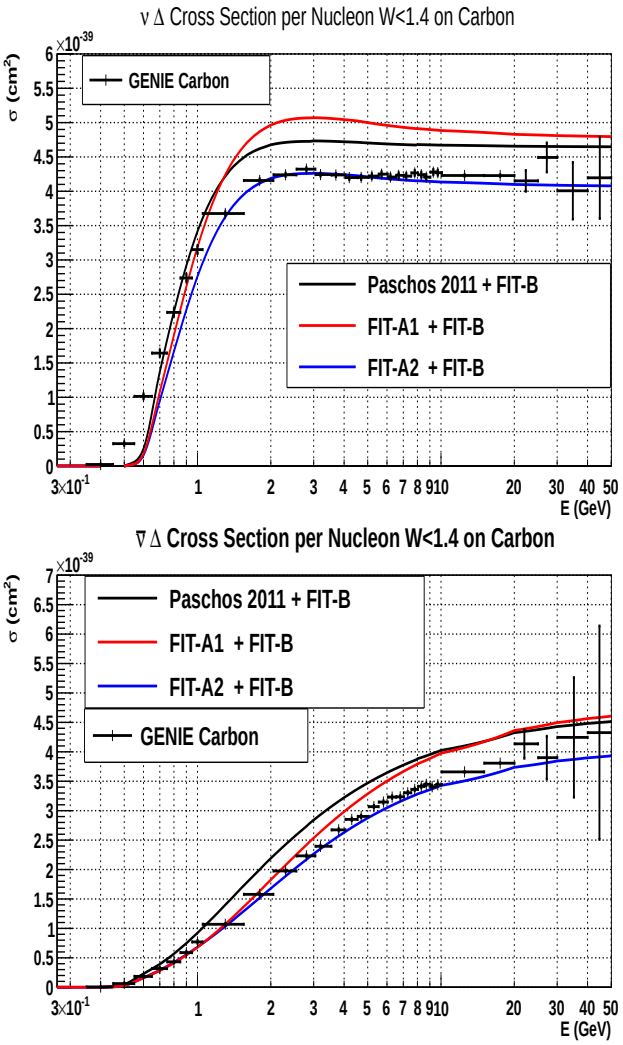

Fig. 22. The total cross sections on carbon (per nucleon) predicted by GENIE for $W < 1.4$ GeV (black points with MC statistical errors) for $\nu_\mu C \to (\mu^- \Delta^{++}$ or $\Delta^+)$ are shown on the top panel, and for $\bar{\nu}_\mu C \to \mu^+ (\Delta^0$ or $\Delta^-)$ are shown on the bottom panel. The GENIE cross section predictions for the total $\Delta(1232)$ production cross sections on carbon fall near the lower bound of our three parametrizations of the experimental data (color online).

6.3 Comparisons of $W < 1.4$ GeV cross sections on carbon

A more relevant comparison is to determine how well the GENIE Monte Carlo describes the sum of the proton and neutron cross sections on carbon, since it is the total number of $\nu < 0.5$ GeV events on carbon that are used in the determination of the neutrino flux.

Fig. 22 shows the predictions from the GENIE MC for total Δ production cross section for $W < 1.4$ GeV on carbon (per nucleon). The neutrino cross sections for $\nu_\mu C \to \mu^- (\Delta^{++}$ or $\Delta^+)$ are shown in the top panel, and the antineutrino cross sections $\bar{\nu}_\mu C \to (\mu^+ \Delta^0$ or $\Delta^-)$ are shown in the bottom panel. The cross sections which are predicted by GENIE are compared to our three parametrizations. (Paschos-2011, FIT-A1 and FIT-A2 for Δ^{++} and Δ^-, and FIT-B for Δ^+ and Δ^0). The GENIE cross section predictions for the total Δ production cross sections on carbon (which use the Rein and Sehgal model[37] for resonance production) fall near the lower bound of our three parametrizations of the experimental data.

6.4 Determination of neutrino and antineutrino flux using $\nu < 0.5$ GeV samples on carbon

The $\nu < 0.5$ GeV sample includes both QE $\nu_\mu N \to \mu^- P$ events ($\approx 66\%$) and Δ production events ($\approx 33\%$).

The top panel of Fig. 23 shows the total correction factor $f_C(E)$ for the $\nu < 0.5$ GeV sample (defined as $f_{C:\nu<0.5}(E)$) for **neutrino** running. Also shown are the various contributions to $f_{C:\nu<0.5}(E)$ including the kinematic correction to $\mathcal{W}_2$ (f_2), and the contributions from $\mathcal{W}_1$ (f_1), $\mathcal{W}_3$ (f_3), $\mathcal{W}_4$ (f_4), and $\mathcal{W}_5$ (f_5). The bottom panel shows the fractional contribution of $\nu < 0.5$ GeV events to the charged current neutrino total cross section. Using our nominal model (TE model for QE scattering and the Paschos 2011 model for Δ production) we find

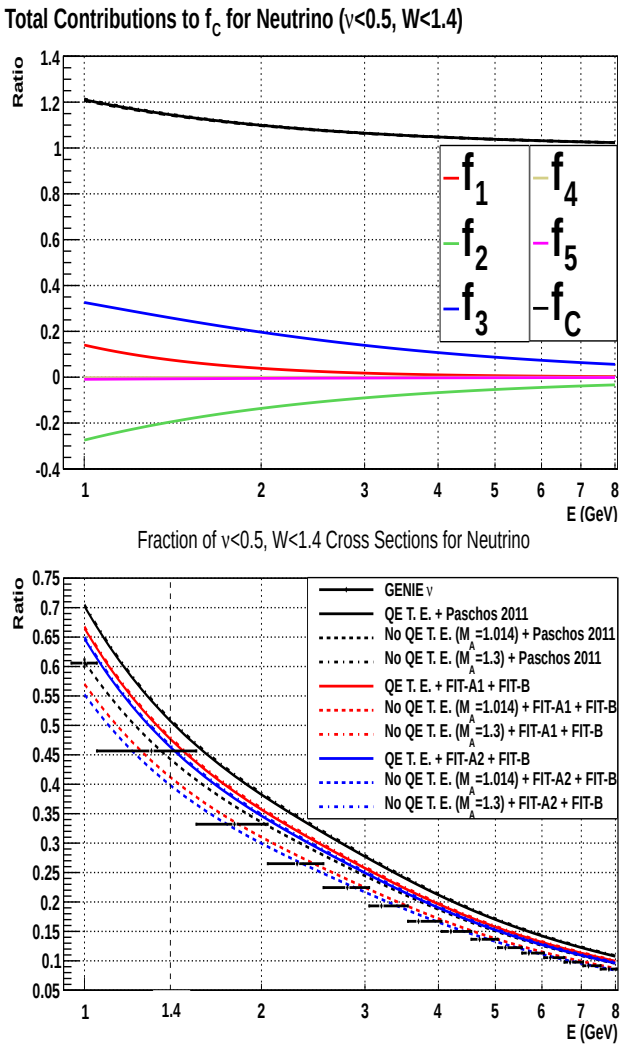

Fig. 23. The $\nu < 0.5$ GeV sample for ν_μ. This sample includes both QE $\nu_\mu N \to \mu^- P$ events (≈66%) and Δ production events (≈ 33%). Top panel: The total corrections factor f_C (with error bands) and the contributions of the kinematic correction to $\mathcal{W}_2$ (f_2), and the contributions from $\mathcal{W}_1$ (f_1), $\mathcal{W}_3$ (f_3), $\mathcal{W}_4$ (f_4), and $\mathcal{W}_5$ (f_5). Bottom panel: The fractional contribution of $\nu <$ 0.5 GeV events to the total cross section. Using our nominal model (QE with transverse enhancement and the Paschos 2011 model for Δ production, shown as the black line), we find that the fraction of $\nu < 0.5$ GeV events is less than 60% for ν_μ energies above 1.2 GeV (color online).

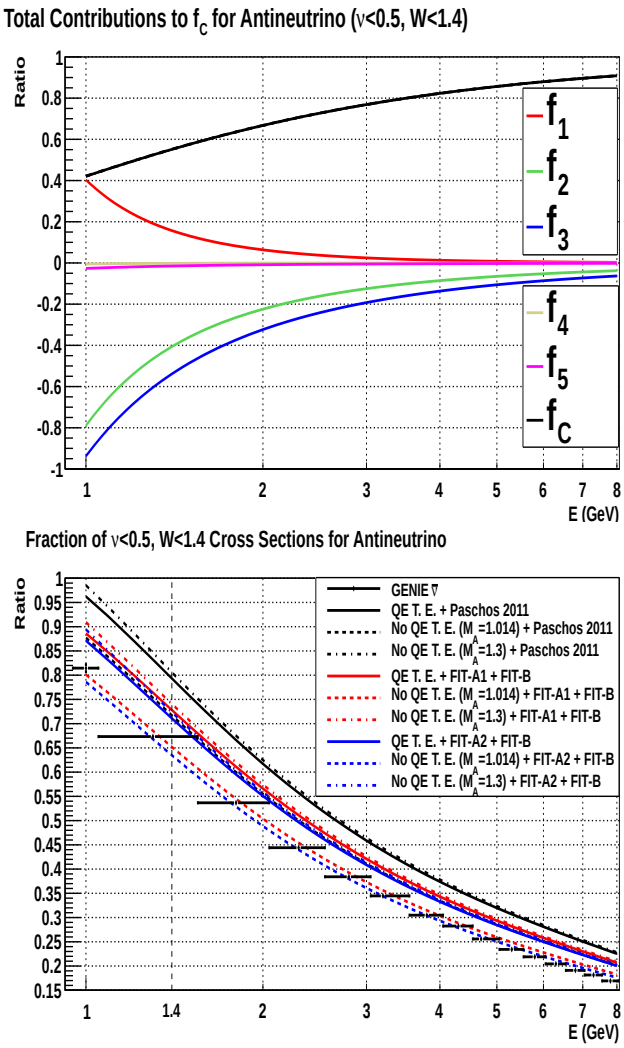

Fig. 24. The $\nu < 0.5$ GeV sample for $\bar{\nu}_\mu$. This sample includes both QE $\bar{\nu}_\mu P \to \mu^+ N$ events (≈66%) and Δ production events (≈33%). Top panel: The total corrections factor f_C and the contributions of the kinematic correction to $\mathcal{W}_2$ (f_2), and the contributions from $\mathcal{W}_1$ (f_1), $\mathcal{W}_3$ (f_3), $\mathcal{W}_4$ (f_4), and $\mathcal{W}_5$ (f_5). Bottom panel: The fractional contribution of $\nu < 0.5$ GeV events to the total cross section. Using our nominal model (TE model for QE scattering and the Paschos 2011 model for Δ production) we find that the fraction of $\nu < 0.5$ GeV events is less than 60% for $\bar{\nu}_\mu$ energies above 2 GeV (color online).

that the fraction of $\nu < 0.5$ GeV events is less than 60% for ν_μ energies above 1.2 GeV.

The top panel of Fig. 24 shows the total correction factor $f_{C:\nu<0.5}(E))$ for **antineutrino** running. Also shown are the various contributions to $f_{C:\nu<0.5}$ including the kinematic correction to $\mathcal{W}_2$ (f_2), and the contributions from $\mathcal{W}_1$ (f_1), $\mathcal{W}_3$ (f_3), $\mathcal{W}_4$ (f_4), and $\mathcal{W}_5$ (f_5). The bottom panel shows the fractional contribution of $\nu < 0.5$ GeV events to the charged current antineutrino total cross section. Using our nominal model (TE model for QE scattering and the Paschos 2011 model for Δ production) we find that the fraction of $\nu < 0.5$ GeV events is less than 60% for $\bar{\nu}_\mu$ energies above 2 GeV.

As for the $\nu < 0.25$ sample, we propose that the neutrino and antineutrino cross sections at low energy be measured relative to the cross sections at 15.1 GeV. Therefore, we define normalized quantity $\bar{f}_{C:\nu<0.5}(15.1)(E)$ for the $\nu < 0.5$ sample as:

$$\bar{f}_{C:\nu<0.5}(15.1)(E) = \sigma_{\nu<0.5}(E)/\sigma_{\nu<0.5}(E = 15.1\ GeV)$$

which is equivalent to

$$\bar{f}_{C:\nu<0.5}(15.1)(E) = f_C(E)/f_C(E = 15.1\ GeV)$$

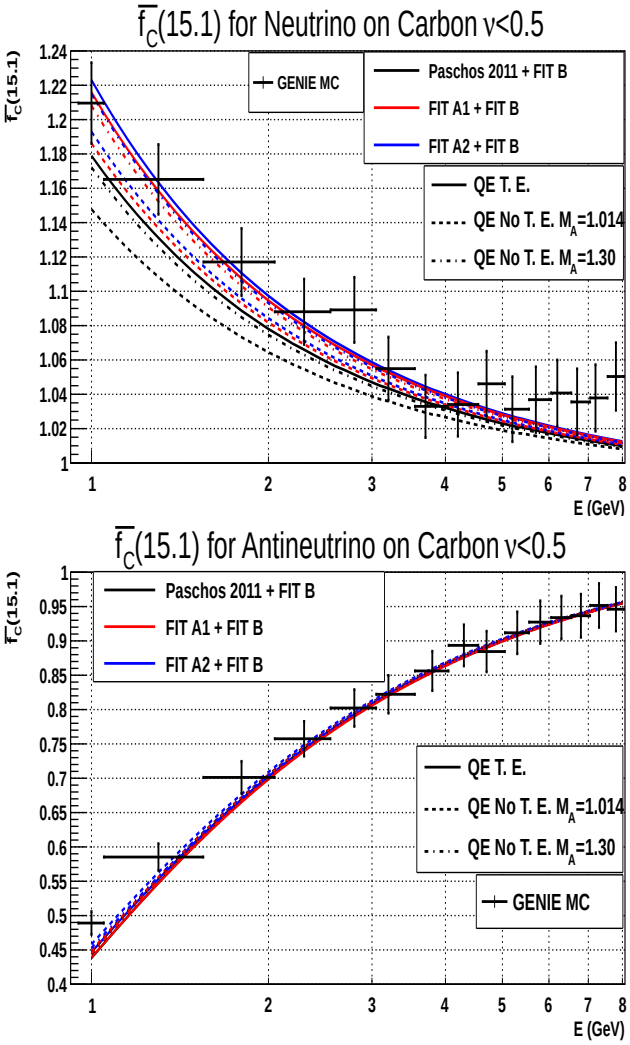

Fig. 25. Comparisons of our calculated values of the normalized $\bar{f}_{C:\nu<0.5}(15.1)(E)$ ($=\bar{f}_C(15.1)$ for $\nu < 0.5$ GeV) to values from the GENIE MC. Our nominal model (shown as the solid black line) uses the TE model for QE scattering and the Paschos 2011 model for Δ production. Neutrinos are shown on the top panel and antineutrinos are shown on the bottom panel (color online).

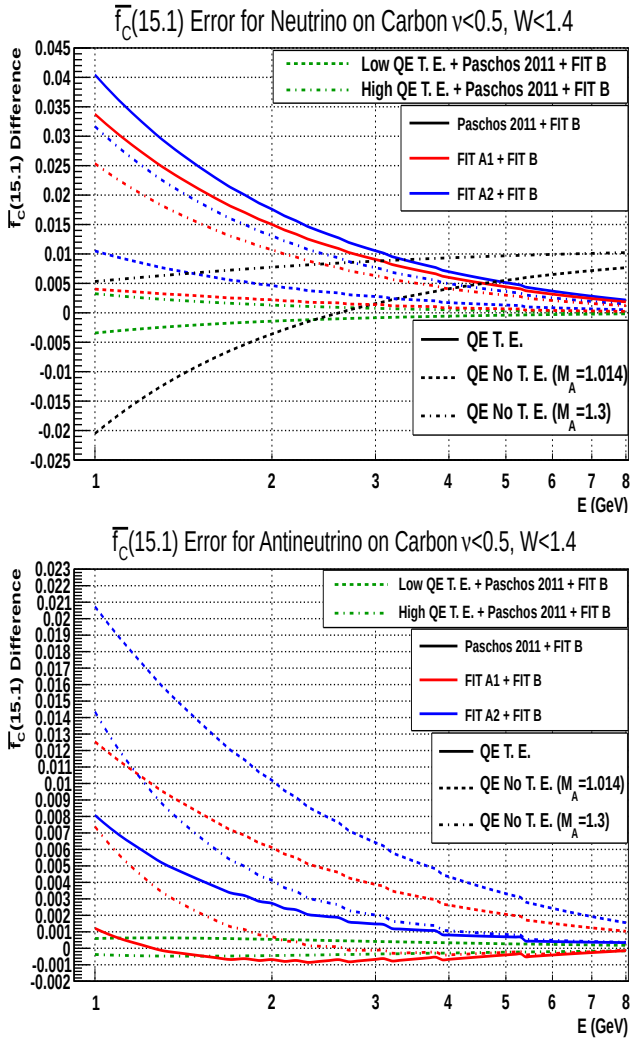

Fig. 26. The error band in the normalized correction factor $\bar{f}_{C:\nu<0.5}(15.1)(E)$ ($=\bar{f}_C(15.1)$ for $\nu < 0.5$ GeV). Our nominal model is QE with transverse enhancement and the Paschos 2011 model for Δ production. Shown are the differences between our nominal model and other model assumptions for neutrinos (top panel) and for antineutrinos (bottom panel). For neutrinos with energies greater than 1.2 GeV, the error in $\bar{f}_C(15.1)$ is less than 0.03, which corresponds to a 2.6% upper limit on the uncertainty in the neutrino flux. For antineutrinos with energies greater than 2 GeV the error in $\bar{f}_C(15.1)$ is less than 0.01 (which corresponds to a 1.4% upper limit on the uncertainty in the antineutrino flux (color online).

The values of $f_{C:\nu<0.5}$(E=15.1 GeV)=1.0113(for ν) and 0.9507 (for $\bar{\nu}$). These values can be used to convert between $\bar{f}_{C:\nu<0.5}(E)$ and $f_{C:\nu<0.5}(E)$.

Fig. 25 show comparisons of our calculated values of the normalized $\bar{f}_{C:\nu<0.5}(15.1)(E)$ (shown as the solid black line) to values extracted from the GENIE MC. The values are calculated from our nominal model which uses the TE model for QE scattering and the Paschos 2011 model for Δ production. Neutrinos are shown on the top panel and antineutrinos are shown on the bottom panel (color online).

Figure 26 shows the error band in the correction factor $\bar{f}_{C:\nu<0.5}(15.1)(E)$ for neutrinos (top panel) and antineutrinos (bottom panel). The error band is defined as the differences between our nominal model and other model assumptions. For neutrinos with energies greater than 1.2 GeV, the error in $\bar{f}_C(15.1)$ is less than 0.03, which corresponds to a 2.6% upper limit on the model uncertainty in the neutrino flux extracted from the $\nu < 0.5$ GeV sample. For antineutrinos with energies greater than 2 GeV the error in $\bar{f}_C(15.1)$ is less than 0.01 (which corresponds to a 1.4% upper limit on the model uncertainty in the antineutrino flux extracted from the $\nu < 0.5$ GeV sample.

In order to go to lower neutrino and antineutrino energies we need to use the $\nu < 0.25$ GeV sample. The model uncertainty in the relative flux extracted from the $\nu < 0.25$

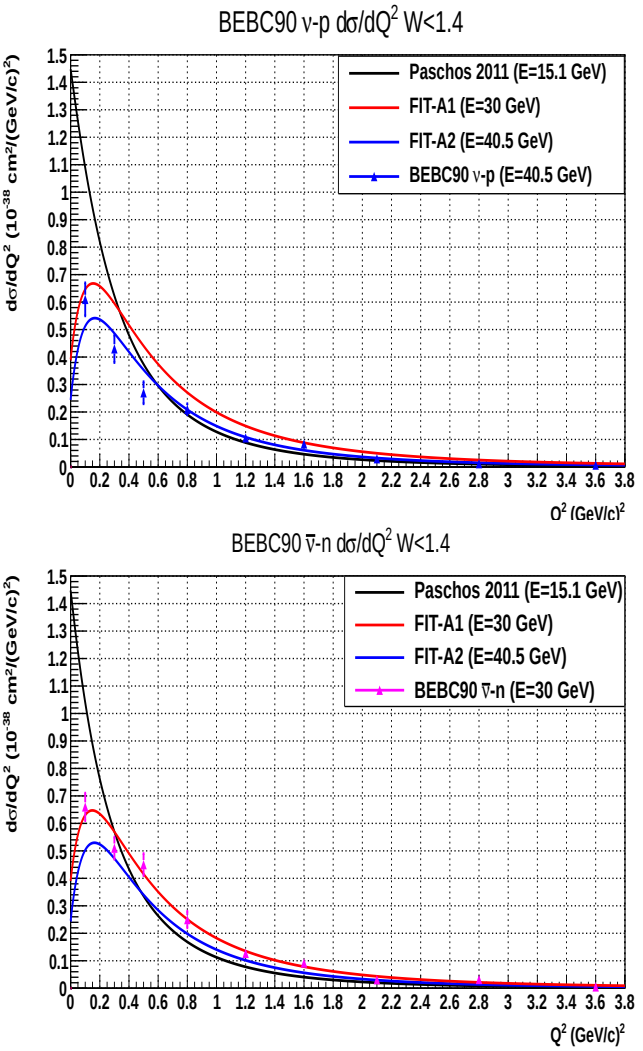

Fig. 27. $d\sigma/dQ^2$ cross sections (for $W < 1.4$ GeV) measured on deuterium at high energies by Allasia et al. (BEBC90[32]). The cross sections for for $\nu_\mu P \rightarrow \mu^- \Delta^{++}$ are shown on the top panel and the cross sections for $\bar{\nu}_\mu N \rightarrow \mu^+ \Delta^-$ are shown on the bottom panel. These two reactions should be described by the same form factors. The black curve labeled Paschos-2011(M_A^Δ=1.05, $C_5^A = 1.2$) is from fits to lower energy $\nu_\mu P$ data (BNL and Argonne). The red curve labeled FIT-A1 (M_A=1.93, $C_5^A = 0.62$) is a fit to the BEBC90 $\bar{\nu}_\mu N$ data on the bottom panel. The blue curve labeled FIT-A2 (M_A=1.75, $C_5^A = 0.49$) is a fit to the BEBC90 $\nu_\mu P$ data on the top panel. The variation among the three curves is taken as a systematic error. (color online).

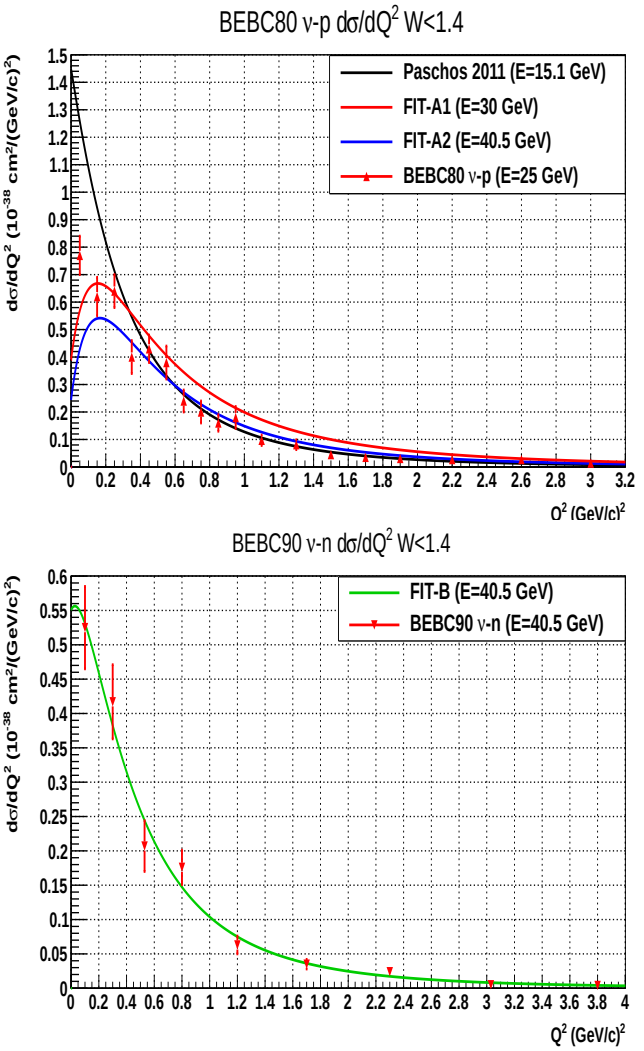

Fig. 28. Top panel: $d\sigma/dQ^2$ for $\nu_\mu P \rightarrow \mu^- \Delta^{++}$ cross sections (for $W < 1.4$ GeV) measured on hydrogen at high energies by Allen et. al. (BEBEC80[31]). The black curve labeled Paschos-2011(M_A^Δ=1.05, $C_5^A = 1.2$) is from fits to low energy $\nu_\mu P$ data (BNL and Argonne). The red curve labeled FIT-A1 (M_A=1.93, $C_5^A = 0.62$) and the blue curve labeled FIT-A2 (M_A=1.75, $C_5^A = 0.49$) are from fits to high energy Allasia et al. (citeBEBC90) data on deuterium. The variation among the three curves is taken as a systematic error. Bottom panel: $d\sigma/dQ^2$ for $\nu_\mu N \rightarrow \mu^- \Delta^+$ cross sections (for $W < 1.4$ GeV) measured by BEBEC90 on free nucleons on deuterium. The green curve labeled FIT-B (M_A=1.62, $C_5^A = 1.27$) represent a fit to the BEBEC90 $\nu_\mu N$ data (color online).

GeV sample is 1.9% for ν_μ energies above 0.7 GeV and 2.5% for $\bar{\nu}_\mu$ energies above 1.0 GeV. With improved determination of QE and Δ production cross sections (e.g. in MINERvA), the model uncertainties can be further reduced, and the method may be extended to lower energies.

6.5 Resolution, acceptance and radiative corrections

The $\nu < 0.25$ events are primarily QE events with $Q^2 < 2M \times 0.25 \approx 0.45$ GeV^2. We can select either all events with $\nu < 0.25$ GeV or only QE events with $Q^2 < 0.5$ GeV^2

The ratio of the number of reconstructed events with $\nu < 0.25$ (or $Q^2 < 0.5$ GeV^2) in data and MC as a function of energy is proportional to the ratio of the true flux to the simulated flux in the MC. This ratio provides a measure of the relative neutrino flux as a function of energy.

A complete Monte Carlo should include the small contributions from coherent pion production, strange particle production such as QE production of hyperons[38], and radiative corrections[39,40]. The the effects of experimental resolution and acceptance should also be simulated.

At preset the GENIE Monte Carlo includes coherent pion production, but does not include the QE production of hyperons, nor radiative effects.

If the GENIE Monte Carlo is used, then one may wish to weight the rate of QE events (as a function of Q^2) by the ratio of events expected in the TE model to the number of events predicted by the model which is implemented in GENIE (i.e. the "Independent Nucleon" model with $M_A = 0.99$ GeV). In addition, QE production of hyperons and radiative effects need to be added.

7 Conclusions

We find the the model uncertainties in using the low ν event samples with $\nu < 0.25$ and $\nu < 0.5$ GeV are well under control (less than 3%). Therefore, the low ν technique can be used at low energies (0.7 GeV for neutrinos and 1 GeV for antineutrinos). Once data from MINErVA on QE scattering and resonance production becomes available, the model uncertainties can be made even smaller, and the technique may be extended to even lower energies.

Since the model uncertainties are under control, the dominant systematic error originates from how well the detector response is understood, Specifically, the mis- reconstuction of high ν events as low ν events must be modeled reliably. This is because at high energies (as shown in Fig. 2) mis-reconstruction of the hadron energy of high ν events can increase the number of low ν events, while at low energies there are fewer high ν events that can be mis-reconstructed at low ν.

8 Appendix

In appendix we illustrate the inconsistencies between the lower energy and higher energy data for neutrino and antineutrino production of the $\Delta(1232)$ resonance. We use a range of fits to span the systematic error in our modeling of Δ production cross sections.

The form factors for $\nu_\mu P \to \mu^- \Delta^{++}$ and $\bar{\nu}_\mu N \to \mu^+ \Delta^-$ should be the same. The $d\sigma/dQ^2$ differential cross sections ($W < 1.4$ GeV) for $\nu_\mu P \to \mu^- \Delta^{++}$ measured at high energies are shown in the top panel of Fig. 27 (Allasia et. al., BEBC90[32] data on deuterium) and also on the top panel of Fig. 28 (Allen et. al. BEBC80[31] data on hydrogen) The bottom panel of Fig. 27 show the $d\sigma/dQ^2$ cross sections at high energies ($W < 1.4$ GeV) for $\bar{\nu}_\mu N \to \mu^+ \Delta^-$ measured by Allasia et. al. (BEBC90) data on deuterium. The black curve labeled Paschos-2011(M_A^Δ=1.05, $C_5^A = 1.2$) is from fits to lower energy $\nu_\mu P \to \mu^- \Delta^{++}$ data (BNL and Argonne). The red curve labeled FIT-A1 (M_A=1.93, $C_5^A = 0.62$) is a fit to the BEBC90 $\bar{\nu}_\mu N \to \mu^+ \Delta^-$ data . The blue curve labeled FIT-A2 (M_A=1.75, $C_5^A = 0.49$) is a fit to the BEBC90 $\nu_\mu P \to \mu^- \Delta^{++}$ data. The variation among the three curves is taken as a systematic error.

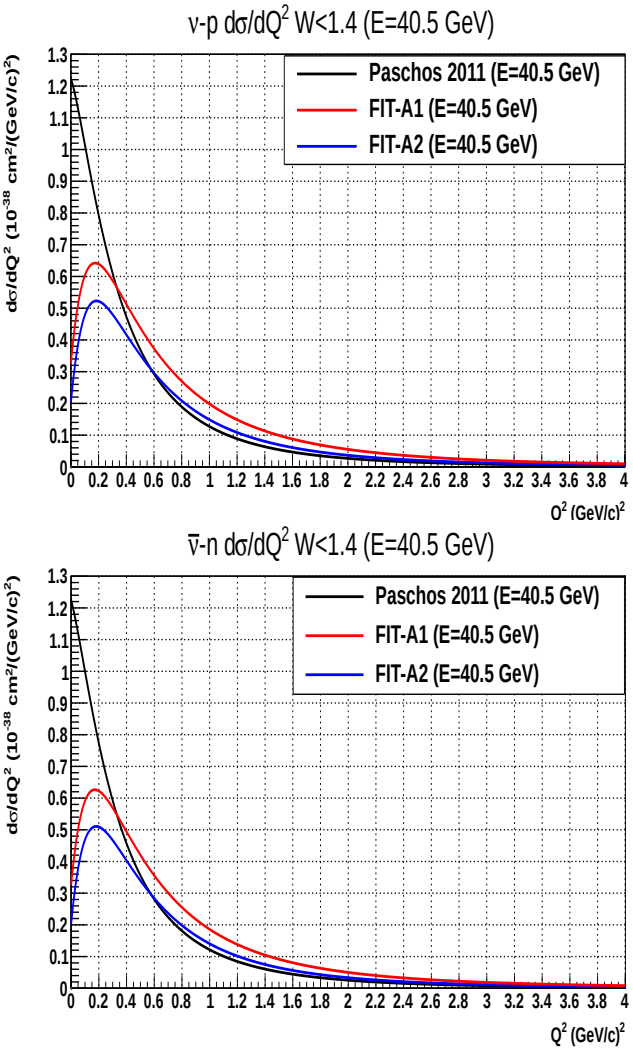

Fig. 29. The three $\nu_\mu P/\bar{\nu}_\mu N$ $d\sigma/dQ^2$ cross sections models (for $W < 1.4$ GeV) with Pauli suppression for nuclear targets at an energy of 40.5 GeV. The cross sections for for $\nu_\mu P \to \mu^- \Delta^{++}$ are shown on the top panel and the cross sections for $\bar{\nu}_\mu N \to \mu^+ \Delta^-$ are shown on the bottom panel. These two reactions should be described by the same form factors. The black curve labeled Paschos-2011(M_A^Δ=1.05, $C_5^A = 1.2$) is from fits to lower energy $\nu_\mu P$ free nucleon data (BNL and Argonne). The red curve labeled FIT-A1 (M_A=1.93, $C_5^A = 0.62$) is a fit to the BEBC90 $\bar{\nu}_\mu N$ free nucleon data. The blue curve labeled FIT-A2 (M_A=1.75, $C_5^A = 0.49$) is a fit to the BEBC90 $\nu_\mu P$ free nucleon data. The variation among the three curves is taken as a systematic error. (color online).

Bottom panel of Fig. 28 shows values of $d\sigma/dQ^2$ differential cross sections for $\nu_\mu N \to \mu^- \Delta^+$ (for $W < 1.4$ GeV) measured by BEBEC90 on free nucleons on deuterium. This reaction has different form factors then $\nu_\mu P \to \mu^- \Delta^{++}$. The green curve labeled FIT-B (M_A=1.62, $C_5^A = 1.27$) represent a fit to the BEBEC90 $\nu_\mu N$ data (color online).

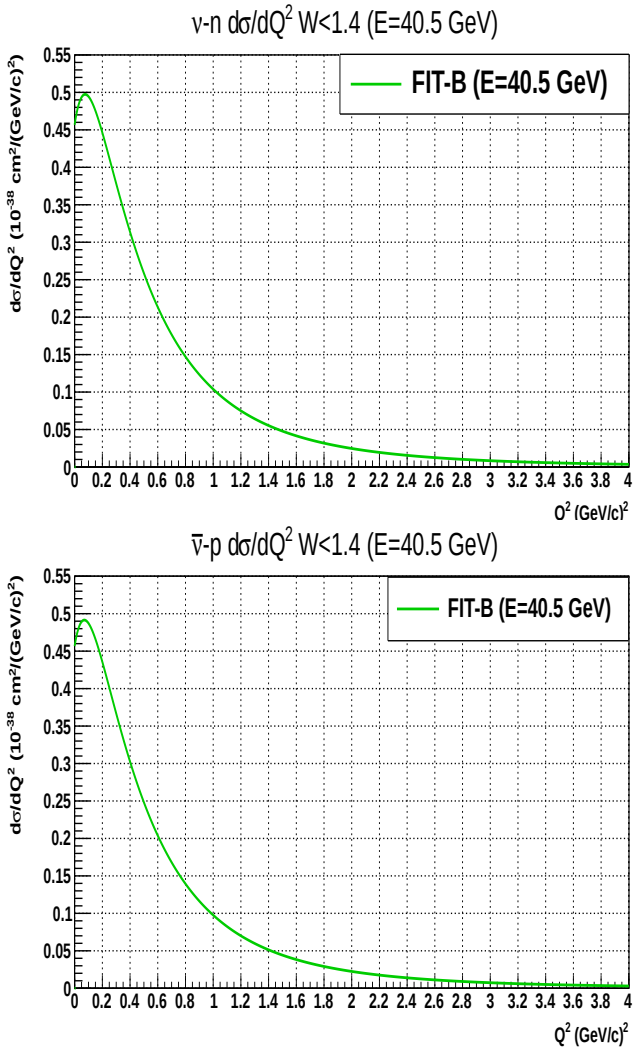

Fig. 30. Our $d\sigma/dQ^2$ cross sections model (for $W < 1.4$ GeV) with Pauli suppression for nuclear targets at an energy of 40.5 GeV. The cross sections for for $\nu_\mu N \to \mu^+ \Delta^-$ are shown on the top panel and the cross sections for $\bar{\nu}_\mu P \to \mu^+ \Delta^0$ are shown on the bottom panel. The green curve labeled FIT-B (M_A=1.62, $C_5^A = 1.27$) represent a fit to the BEBEC90 $\nu_\mu N$ free nucleon data (color online).

We use the above models with the addition of Pauli suppression in order to model the differential cross sections on nuclear targets.

Fig. 29 shows our three $\nu_\mu P/\bar{\nu}_\mu N$ $d\sigma/dQ^2$ cross sections models (for $W < 1.4$ GeV) with Pauli suppression for nuclear targets at an energy of 40.5 GeV. The cross sections for for $\nu_\mu P \to \mu^- \Delta^{++}$ are shown on the top panel and the cross sections for $\bar{\nu}_\mu N \to \mu^+ \Delta^-$ are shown on the bottom panel. These two reactions should be described by the same form factors. The black curve labeled Paschos-2011(M_A^Δ=1.05, $C_5^A = 1.2$) is from fits to lower energy $\nu_\mu P$ free nucleon data (BNL and Argonne). The red curve labeled FIT-A1 (M_A=1.93, $C_5^A = 0.62$) is from a fit to the BEBC90 $\bar{\nu}_\mu N$ free nucleon data. The blue curve labeled FIT-A2 (M_A=1.75, $C_5^A = 0.49$) is from a fit to the BEBC90 $\nu_\mu P$ free nucleon data. The variation among the three curves is taken as a systematic error.

Fig. 30 shows our $\nu_\mu N/\bar{\nu}_\mu P$ $d\sigma/dQ^2$ cross sections model (for $W < 1.4$ GeV) with Pauli suppression for nuclear targets at an energy of 40.5 GeV. The cross sections for for $\nu_\mu N \to \mu^+ \Delta^-$ are shown on the top panel and the cross sections for $\bar{\nu}_\mu P \to \mu^+ \Delta^0$ are shown on the bottom panel. The green curve labeled FIT-B (M_A=1.62, $C_5^A = 1.27$) is extracted fit to the BEBEC90 $\nu_\mu N$ free nucleon data.

8.1 Δ production form factors

For the vector contribution we use the formulae for $\mathcal{W}_1, \mathcal{W}_2, \mathcal{W}_3, \mathcal{W}_4,$ free nucleons from Lalakulich and Paschos[10]. We neglect the effect of Fermi motion. The form factors that we use are taken from Paschos and Schalla[10]. Specifically, the vector form factors are

$$C_3^V(Q^2) = \frac{2.13/D_V}{1+\frac{Q^2}{4M_V^2}} \quad , \quad C_4^V(Q^2) = \frac{-1.51/D_V}{1+\frac{Q^2}{4M_V^2}} \quad (15)$$

$$C_5^V(Q^2) = \frac{0.48/D_V}{1+\frac{Q^2}{0.776M_V^2}} \quad \text{and} \quad D_V = \left(1+\frac{Q^2}{M_V^2}\right)^2 \quad (16)$$

with $M_V = 0.84$ GeV, which have been extracted from electroproduction data.

For the vector-axial interference $W_3(Q^2,\nu)$ Paschos and Schalla use the form factor $C_5^A(Q^2)$ $C_5^A(Q^2) = \frac{C_5^A}{(1+Q^2/M_A^2)^2}\frac{1}{1+2Q^2}$ where $C_5^A(0)$ is defined as C_5^A, and $C_4^A = -\frac{1}{4}C_5^A$

Paschos and Schalla use low energy $\pi^+ p \to \Delta^{++}$ where the non-resonant background is smallest. With M_A=1.05 GeV they extract value of $C_5^A(0) = 1.08$ from the data. Since this value is close to 1.20 predicted by the Goldberger-Treiman relation, they chose to use C_5^A=1.2.

For Δ^{++} and Δ^- we define the Pachos-2011 parameterization using above form factors with C_5^A=1.2 (extracted through PCAC), M_A=1.05 GeV, and the vector form factors described above. As mentioned earlier, FIT-A1 and FIT-A2 use the same form but with different values of C_5^A and M_A.

For Δ^+ and Δ^0 production our Fit-B uses the the same form factors multiplied by a factor of $1/\sqrt{(3)}$ (as expected[10] from Clebsch-Gordan coefficients). However, in order to account for the large non-resonance background, we use different values C_5^A and M_A.

Paschos and Schalla mention that several recent articles also calculate $C_5^A(0)$ by fitting experimental data [41–47] with their values varying from 0.87 up to 1.20. Models with a resonant background [41,42] prefer the power value, while the other articles [43–47] prefer values closer to 1.20. The reasons for the differences is the treatment of the non-resonant background, the form of the axial form factor that is used, and the exact kinematics at small Q^2.

References

1. Y. Itow et al., (T2K) arXiv:hep-ex/0106019;
2. D.G. Michael et al., (MINOS) Phys. Rev. Lett. **97**, 191801 (2006); http://www-numi.fnal.gov/Minos/
3. P. Adamson et al., (MINOS) Phys. Rev. D **81**, 072002 (2010).
4. http://www-nova.fnal.gov/
5. http://minerva.fnal.gov/
6. S. R. Mishra, in *Proceedings of the Workshop on Hadron Structure Functions and Parton Distributions* , edited by D. Geesaman *et al*
7. W. Seligman, Ph.D. thesis, Columbia University, 1997), Nevis 292.
8. H. Gallagher, (NEUGEN) Nucl. Phys. Proc. Suppl. 112 (2002).
9. D. Bardin and V. Dokuchaeva, Preprong JINR-E2-86-260 (1986).
10. O. Lalakulich and E. A. Paschos, Phys. Rev. D **71**, 074003 (2005), and Phys. Rev. D **74**,014009 (2006); E. A. Paschos and D. Schalla, Phys. Rev. D **84**, 013004 (2011))
11. E. A. Paschos and J. Y. Yu, Phys. Rev. D **65**:033002 (2002).
12. C.Andreopoulos (GENIE), Nucl. Instrum. Meth.A614, 87,2010; H. Gallagher, (NEUGEN) Nucl. Phys. Proc. Suppl. 112 (2002);Y. Hayato (NEUT), Nucl Phys. Proc. Suppl.. **112**, 171 (2002);D. Casper (NUANCE) , Nucl. Phys. Proc. Suppl. 112, 161 (2002); http://nuint.ps.uci.edu/nuance/
13. C. H. Llewellyn Smith, Phys. Rep. 3C (1972); E. A. Paschos, Electroweak Theory, Cambridge University Press (2007).
14. A. Bodek, H. Budd and E. Christy, Eur.Phys. J. **C**71, 172 (2011)
15. F.M. Steffens and K. Tsushima , Phys. Rev. D **70**, 094040 (2004)
16. J. Carlson, J. Jourdan, R. Schiavilla, and I. Sick, Phys. Rev. C **65** 024002 (2002)
17. A. Bodek, S. Avvakumov, R. Bradford, and H. Budd, Eur. Phys. J. C**53**, 349 (2008).
18. JUPITER collaboration, Jefferson Lab experiment E04-001, Arie Bodek, Cynthia Keppel and M. Eric Christy, spokespersons.
19. V. Mamyan, Ph.D. dissertation, University of Virginia, 2010.
20. M. Martini, M. Ericson, G. Chanfray, and J. Marteau, Phys. Rev. C 80: 065501, 2009; ibid Phys. Rev. C 81: 045502, 2010.
21. A. A. Aguilar-Arevalo et al., (MiniBooNE) Phys. Rev. Lett **98**, 231801(2007); A.A. Aguilar-Arevalo *et al.* Measurement of the neutrino component of an anti-neutrino beam observed by a non-magnetized detector. e-Print: arXiv:1102.1964 [hep-ex]
22. V. Lyubushkin et al. (NOMAD Collaboration), Eur. Phys. J. C **63**, 355 (2009); Q. Wu *et al.*(NOMAD Collaboration), Phys. Lett. **B60**, 19 (2008).
23. V.B. Anikeev, et al. (Serpukhov) Z. Phys. C **70**, 39 (1996)
24. N. J. Baker et al. (BNL) Phys. Rev. D **25**, 617 (1982).
25. J. Campbell et. al. (ANL), Phys. Rev. Lett. **30**, 335 (1973)
26. S. J. Barish et al. (ANL) Phys. Rev. D **19**, 2521 (1979)
27. G.M. Radecky et al. (ANL) Phys. Rev. D **25**, 1161 (1982)
28. T. Kitagaki et al. (BNL) Phys. Rev. D **34**, 2554 (1986)
29. J. Bell 1978 et al. (FNAL) Phys. Rev. Lett. **41**, 1008 (1978); ibid 1012 (1978)
30. V.I. Efremenko et al. (FNAL) ITEP-83-1981 (unpublished).
31. P. Allen et al. (BEBC) , Nucl. Phys. B176, 269(1980); ibid B**264** ,221 (1986)
32. D. Allasia et al. (BEBC), Nucl. Phys. B **343**, 285 (1990).
33. W. Lerche et al. (GGM) Phys.Lett. B**78**, 510 (1978)
34. V.V. Ammosov et al (SKAT) Soviet J. Nucl. Phys. **50** ,57 (1988)
35. H. J. Grabosch et. al. (SKAT) Z. Phys. C **41**, 527 (1989)
36. T. Bolognese et al. (GGM) Phys. Lett. B **81**, 393 (1979)
37. D. Rein and L. M. Sehgal, Annals Phys. **133** 79 (1981); R. Belusevic and D. Rein, Phys. Rev. D **46**, 3747 (1992)
38. V.V. Ammosov et al. (FNAL E180) JETP Lett.43 716,1986, Pisma Zh.Eksp.Teor.Fiz.43 554,1986.
39. J. Kiskis, Phys. Rev. **D8** 2129 (1973); Roger J. Barlow and Stephen Wolfram, Phys. Rev. **D20** 2198 (1979); A.B. Arbuzov , D.Yu. Bardin, L.V. Kalinovskaya hep-ph/0407203) JHEP 0506 (2005).
40. A. De Rújula, R. Petronzio, and A. Savoy-Navarro, Nucl. Phys. B **154**, 394 (1979); Gunther Sigl, Phys. Rev. **D57** 3786 (1998); A. Bodek, " Muon internal bremsstrahlung: A Conventional explanation for the excess nu(e) events in MiniBoone" , arXiv:0709.4004 [hep-ex]
41. E. Hernandez, J. Nieves, and M. Valverde, Phys. Rev. **D76**, 033005 (2007), hep-ph/0701149.
42. O. Lalakulich, T. Leitner, O. Buss, and U. Mosel, Phys. Rev. **D82**, 093001 (2010), 1007.0925.
43. T. Leitner, O. Buss, L. Alvarez-Ruso, and U. Mosel, Phys. Rev. **C79**, 034601 (2009), 0812.0587.
44. K. M. Graczyk, D. Kielczewska, P. Przewlocki, and J. T. Sobczyk, Phys. Rev. **D80**, 093001 (2009), 0908.2175.
45. E. Hernandez, J. Nieves, M. Valverde, and M. J. Vicente Vacas, Phys. Rev. **D81**, 085046 (2010), 1001.4416.
46. L. Alvarez-Ruso, S. K. Singh, and M. J. Vicente Vacas, Phys. Rev. **C59**, 3386 (1999), nucl-th/9804007.
47. M. Sajjad Athar, S. Chauhan, and S. K. Singh, J. Phys. **G37**, 015005 (2010), 0908.1442.
48. G. M. Radecky *et al.*, Phys. Rev. **D25**, 1161 (1982).